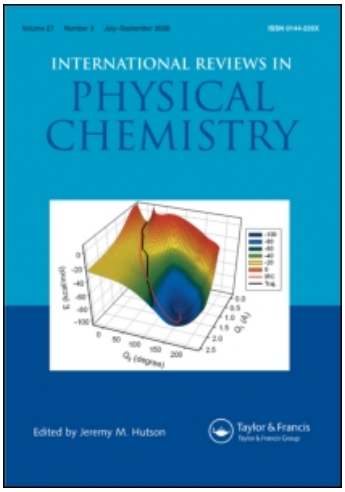

International Reviews in Physical Chemistry
Publication details, including instructions for authors and subscription information:
http://www.informaworld.com/smpp/title~content=t713724383

Beyond single particle mass spectrometry: multidimensional characterisation of individual aerosol particles

Alla Zelenyuk[a]; Dan Imre[b]
[a] Pacific Northwest National Laboratory, Richland, WA 99354, USA [b] Imre Consulting, Richland, WA 99352, USA

To cite this Article Zelenyuk, Alla and Imre, Dan(2009) 'Beyond single particle mass spectrometry: multidimensional characterisation of individual aerosol particles', International Reviews in Physical Chemistry, 28: 2, 309 — 358
To link to this Article: DOI: 10.1080/01442350903037458
URL: http://dx.doi.org/10.1080/01442350903037458

International Reviews in Physical Chemistry
Vol. 28, No. 2, April–June 2009, 309–358

Taylor & Francis
Taylor & Francis Group

Beyond single particle mass spectrometry: multidimensional characterisation of individual aerosol particles

Alla Zelenyuk[a]* and Dan Imre[b]

[a]*Pacific Northwest National Laboratory, Richland, WA 99354, USA;* [b]*Imre Consulting, Richland, WA 99352, USA*

(*Received 15 April 2009; final version received 11 May 2009*)

The behaviour of small aerosol particles depends on a number of their physical and chemical properties, many of which are strongly coupled. The size, internal composition, density, shape, morphology, hygroscopicity, index of refraction, activity as cloud condensation nuclei and ice nuclei and other attributes of individual particles all play a role in determining particle properties and their impacts. The traditional particle characterisation approaches rely on separate parallel measurements that average over an ensemble of particles of different sizes and/or compositions and later attempt to draw correlations between them. As a result such studies overlook critical differences between particles and bulk and miss the fact that individual particles often exhibit major differences. Here, we review the recently developed methods to simultaneously measure *in situ* and in real time several of the attributes for individual particles using a single particle mass spectrometer (SPMS), SPLAT or its second generation SPLAT II. We also discuss novel approaches developed for classification, visualisation and mining of large datasets produced by the multidimensional single particle characterisation.

Keywords: single particle mass spectrometer; vacuum aerodynamic diameter; aerosol composition; particle density; particle shape; aerosol hygroscopicity

Contents

*Corresponding author. Email: alla.zelenyuk@pnl.gov

ISSN 0144–235X print/ISSN 1366–591X online

DOI: 10.1080/01442350903037458
http://www.informaworld.com

1. Introduction

Aerosols are ubiquitous, playing an important role in many areas that have direct impact on our lives. Atmospheric aerosols affect climate, visibility and human health. Aerosol climate forcing remains at present the single largest uncertain quantity in climate models [1,2]. In the medical field aerosols are commonly used for drug delivery and high-resolution imaging. Nanotechnology takes advantage of the uniqueness of the chemical and physical properties of small particles, which as we are finding, are different from those of bulk materials or isolated molecules [3–5], to produce novel materials. And in a post-9/11 world, we must also consider the fact that biological and chemical warfare agents are commonly dispersed through the atmosphere as aerosols. These are a few examples that illustrate the significant role that aerosols play in a wide range of fields. Each of these fields of science and technology could greatly benefit from the development of analytical tools that would make possible measurements of salient aerosol properties on-line and in real-time.

Traditional approaches to small particle characterisation that rely on measurements that average over an ensemble of particles of different sizes and/or compositions miss the critical differences between bulk and particles and, in many cases, fail to obtain a proper measure of some of the most important particle properties. There is a big difference between an aerosol sample that is composed of two types of particles: some containing only compound A and others only compound B, and another sample, whose individual particles are internally mixed, containing both A and B. Since this is true even if the two aerosol samples contain, on average, the same amount of compounds A and B, the ideal instrument for aerosol characterisation should provide information on properties of the individual particles. Given that the two most fundamental properties of particles are their size and composition, this instrument should, at the very least, measure the sizes and compositions of individual particles.

However, in most fields there is a need to know more than just size and composition. For example, in the atmospheric science field, there is a need to establish a connection between particles sizes and compositions and their optical properties, and propensity to act as cloud condensation nuclei (CNN), which are the climatically relevant particle attributes. It is clearly also important to know how particles of various compositions transform in the atmosphere with time, changes in temperature, or relative humidity (RH). This type

of information is typically obtained by an assembly of investigators and instruments that carry out large number of measurements simultaneously on the same parcel of air, but not on the very same particles. These often include a number of chemical analysis techniques, measurements of particle size distributions, light scattering, CCN activity, hygroscopicity, etc. At the conclusion of these multi-investigator studies there is a need to 'connect the dots' and obtain from these independent pieces a simple story, in which particle composition and size are related to aerosol climatic impact.

Our goal was to develop an analytical tool that will make it possible to measure in real-time, *in situ*, simultaneously many of the important properties on the *very same particles*, thereby eliminate the need to 'guess' the relationship between particle size and composition and their salient ambient properties and behaviour. The real-time characterisation of particles, however, presents unique challenges: Typical aerosol number concentrations are between 10^2 and 10^6 particles/cm^3, which, in number concentrations, are significantly lower than the concentrations of trace gas molecules in the ambient atmosphere at their detection limit. Moreover, since the properties of a suspension of particles depends on the internal compositions of the individual particles and often on which of the compounds are on the surface, we have to acknowledge that the true concentration of any type of particles of any given size is significantly smaller than the numbers stated above.

In summary, given that the behaviour and impact of aerosols are functions of individual particles' internal composition, size, shape and morphology, a detailed description of an aerosol sample should ideally be based on particle-by-particle analysis. Single particle mass spectrometers (SPMSs) lead the field of *in situ*, real-time analysis of individual particle size and composition and were described in a review of aerosol measurements [6] as 'arguably, the most significant development in aerosol measurement in the past 20 years'. The knowledge gained through deployments of various SPMSs' designs, both in the laboratory and in the field, has undeniably proven to be extremely valuable [7–12]. But SPMSs have also persistently been subject to criticism on a number of fronts, most of which relate to their inability to yield reliable quantitative data.

A number of recent reviews and tutorials [6,8–11,13–15] provide detailed descriptions and comparisons between the various instrument designs being deployed. Here we mostly focus on SPLAT II [16], our new SPMS, which was designed to directly address many of the shortcomings that are often associated with SPMSs. Compared with other, existing SPMSs, SPLAT II offers significantly improved detection sensitivity, particularly to small particles, unparalleled particle sizing precision, higher sampling rates and hence improved temporal resolution, a method of generating high-quality mass spectra, a size-independent hit rate and increased mass spectral dynamic range, all of which result in significant improvements in the instrument's capability to yield quantitative data.

Why do we feel that improvements in these specific areas were critical? Atmospheric aerosols provide a good example: their size distributions range from a few nanometres to a few microns with the vast majority of the particles being smaller than 200 nm. An unbiased portrayal of the composition of this aerosol requires an instrument with a wide dynamic size range and a sub-100 nm lower size limit. Statistically meaningful sampling of this wide size range, especially on mobile platforms like an aircraft, can only be accomplished with a high sampling rate, which, in turn, requires high instrument sensitivity. And, finally,

quantification of the complex internal compositions routinely observed in the atmosphere requires high-quality mass spectra.

We have already mentioned that it is often important to know in addition to individual particle size and composition other particle properties. As it turns out, the significant improvement in instrument sensitivity and sizing precision opens the door to simultaneous measurements of particle shape [17,18], density [19,20], fractal dimension [21] and even the propensity of particles to interact with water vapour, or hygroscopicity [22–24]. The simultaneous measurement of a number of properties which we term, multi-dimensional particle characterisation provides a wealth of information that directly maps the relationship between these attributes and can also be extended to extract highly quantitative individual particle composition [24,25].

Single particle measurements by their very nature produce vast amounts of detailed data, the mining and analysis of which calls for unconventional approaches that must in some sense draw on statistical methods [26–30], but should ideally preserve the wealth and depth of information that was obtained. The success of SPMSs is critically dependent on having, in addition to high-quality hardware, powerful data analysis and visualisation software packages. Analysis of individual particle mass spectra (IPMS) is a special example of cases, in which massive, complex, multidimensional datasets require matching advances in the science of data organisation, visualisation and mining.

To take full advantage of the vast amounts of data SPLAT II generates we have developed software packages called SpectraMiner [31] and ClusterSculptor [32,33]. The former is a data visualisation and mining program that adopts a very different approach from any other in the field [26–30,34], making it possible to mine datasets of millions of particles without loss of information and explore relationships between different particle classes and between particles and any other data that were concurrently collected. ClusterSculptor uses statistical tools to organise the massive datasets, but places the scientist at the centre of the data classification process by providing him/her with the tools to use scientific knowledge to steer the process. These intuitive visually driven tools can be applied to any large multidimensional datasets and have applications far beyond single particle mass spectrometry.

The review is organised as follows: Section 2 is devoted to the brief overview of SPLAT II 'basics', explaining how it works and illustrating its performance characteristics. Simultaneous measurements of multiple properties of individual particles are reviewed in Section 3. Section 4 presents our approach to classify, visualise and mine large datasets produced by the multidimensional single particle characterisation. Finally, brief conclusions are given in Section 5.

2. SPLAT II: an ultra-sensitive, high-precision SPMS

The vast majority of SPMSs transport particles from the ambient environment into the vacuum using especially designed inlets. Once in vacuum the particles are detected by optical light scattering and sized either by measuring their velocities or on the basis of the intensity of the scattered light. Following particle detection and sizing, a UV laser pulse is triggered to fire synchronously with the particle's arrival at the entrance of the mass spectrometer. The UV laser pulse ablates the particle and a mass spectral signature of the generated ions is recorded. The process is repeated for each particle and individual particle

mass spectra (IPMS) are stored for analysis. As we mentioned above, at present there are a number of SPMS designs, each brings strengths in specific areas [6,8–11,13–15].

Thus far we have designed and constructed two SPMSs; the first, SPLAT [12], served as our test-bed and provided us with experience, on the basis of which the second generation instrument, SPLAT II [16], was designed and constructed. From the outset our goal was to construct a SPMS that offered the following features: high sensitivity, particularly to small particles, which was to be translated to high temporal resolution; highly precise particle sizing and high-quality mass spectra that exhibit limited fragmentation and diminished matrix and charge-transfer effects. While SPLAT II shares some elements with SPLAT, it brings significant improvements in performance, and reduction in size and weight that make it aircraft-compatible. Consequently, in this section we present the design elements and performance of SPLAT II, but the sections that follow contain measurements conducted by both instruments. For simplicity we will refer to both as SPLAT.

Since the intensity of the light scattered by particles decreases extremely rapidly with particle size [35] the optical detection efficiencies of particles that are smaller than ~150 nm in diameter tend to be extremely low [12,36]. Some SPMSs overcome their inability to detect small particles by randomly firing the ablation laser and relying on the rare occurrence of random coincidences when the laser pulse happens to hit a particle. Unfortunately, this approach yields a very low sampling rate [9] and provides no information about particle size [37,38], unless particles are size-classified prior to sampling either aerodynamically or by using a differential mobility analyser (DMA) [39], which in turn further decreases instrument sampling rate and sensitivity.

Figure 1 shows a schematic representation of our SPMS – SPLAT II. It uses an aerodynamic lens inlet to form a very narrow particle beam, with a diameter of a few 100 μm and with very low divergence [40,41]. This inlet makes it possible to transport the particles into the instrument with extremely high efficiency [12,16,42]. It also imparts particles with very narrow velocity distributions that are related to their vacuum aerodynamic diameters (d_{va}), making it possible to determine their size with high precision [12,16]. It is important to point out that one of the consequences of transporting particles from high ambient pressure into the vacuum is that it is accompanied by a rapid drop in RH. Since many atmospheric particles contain some water, this drop in RH during sampling has the potential to result in a significant loss of water from the particles, which affects particle size, transmission efficiency, ionisation probability and mass spectrum. Yet, the vast majority of instruments that deploy this inlet sample particles at the ambient RH and interpret the data under the assumption that no evaporation occurs. We felt that it was imperative to address this issue by conducting a study, under well-defined conditions, to quantify water evaporation from particles during transport in the aerodynamic lens.

The study that was conducted on a range of particles of different sizes and compositions, showed unequivocally that a significant fraction of the water that is in particles evaporates during their transport [43]. We concluded that the only sure way to eliminate ambiguities and generate interpretable and meaningful measurements of vacuum aerodynamic diameter with instruments that use low-pressure aerodynamic lens inlets is to dry the particles prior to their sampling. Note that drying particles does not necessarily guarantee that the particles lose all of their water prior to the measurement. As we will discuss in the section below a number of particle systems are known to retain water even

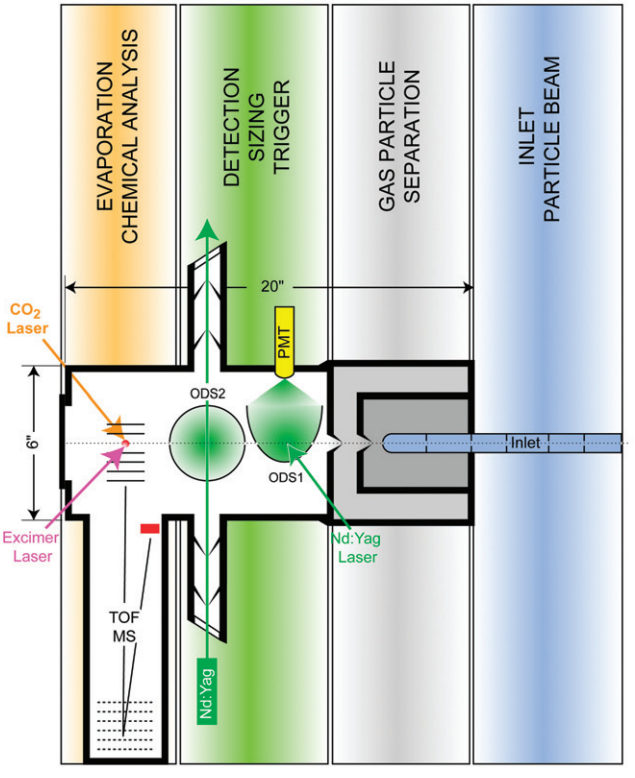

Figure 1. [Colour online] A schematic of SPLAT II [16].

under vacuum conditions. For these particle systems drying ensures that the measurements conducted by all instruments are reproducible and comparable.

After exiting the aerodynamic lens inlet the particles travel through two differentially pumped stages and enter the main, low-pressure chamber, where they pass through two optical detection stages. Each optical stage is equipped with a 300 mW, continuous-wave, green laser that intersects the particle beam at the focal point of a large ellipsoidal reflector. The ellipsoidal reflector is used to collect over 60% of light scattered by the particle when it intersects the green laser beam. The scattered light is detected by a photon counting photomultiplier tube (PMT), and is continuously compared to an operator predetermined photon count threshold. Once the threshold limit is met at the first optical stage, indicating that a particle was detected, a clock is started. At 10.5 cm downstream from the first detection stage, the particle crosses the path of the second green laser and the process is repeated. The time elapsed between the two detection signals yields the particle's velocity from which its vacuum aerodynamic diameter is determined. The particle detection time and the calculated particle velocity are used to synchronise the firing of the evaporation and ionisation lasers with the particle's arrival at the ionisation region of the angular reflectron time-of-flight mass spectrometer. This arrangement ensures high hit-rate and 'background-free' IPMS.

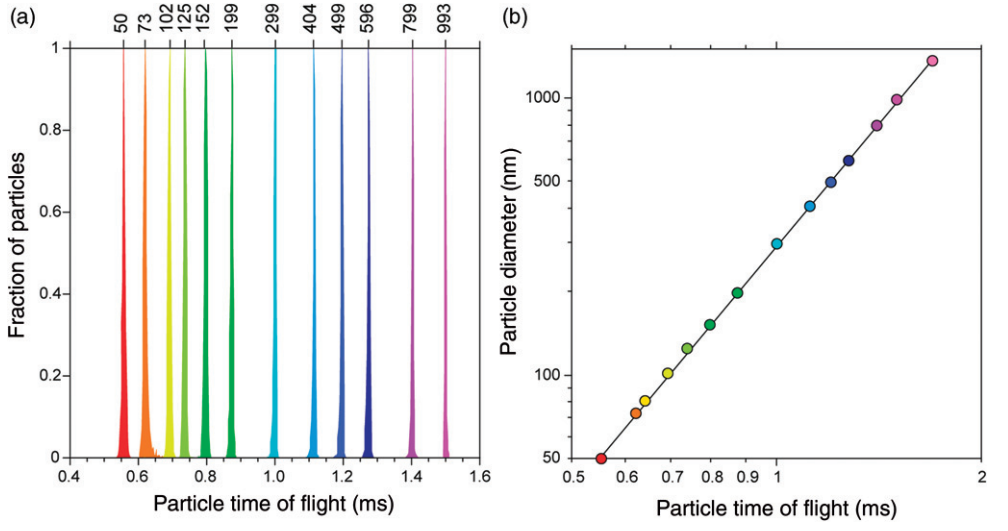

Figure 2. [Colour online] (a) Distributions of particle time of flights for PSL particles with 13 different sizes from 50 to 993 nm; (b) A calibration curve used to convert particle time of flight to vacuum aerodynamic diameter [16].

Figure 2(a) is a plot of the measured particles time-of-flight distributions for NIST certified size standards polystyrene latex (PSL) spheres with diameters from 50 to 993 nm. Figure 2(b) shows the particle time-of-flight to size calibration curve that was generated using the data shown in Figure 2(a). A careful examination of the measured d_{va} distributions shows that for each of these particles the line shape is in accord with the manufacturer-specified size distributions. To date the narrowest line shape measured by SPLAT II has a full width at half maximum (FWHM) of 1.8%. The ability to measure the size of 200 nm particles with this precision translates into a resolution power of about a monolayer [12,16].

As we already mentioned above the light scattering cross-section decreases rapidly as particle size decreases and with it the instrument detection probability. Since one of the most important goals was to construct an instrument that has high sensitivity to small particles, we maximised the detection signal by using scattering lasers of relatively high power and by collecting more than 60% of the scattered light with large elliptical reflectors. To reduce background we have incorporated design elements that minimise stray light, which made it possible to resort to photon counting, enabling detection of very small particles.

Figure 3 presents the results of measurements of particle detection probability as function of particle size for three particle types: spherical PSL beads, size selected, spherical sodium nitrate and aspherical sodium chloride. Instrument detection probability is defined as the ratio of particles detected and properly characterised to the number of particles entering the instrument. Defined in this manner the detection probability is directly related to the instrument performance. Figure 3 shows that the detection of spherical particles with diameters between 125 and 600 nm is very close to 100%. The detection of particles larger than 600 nm decreases slowly because of the decrease

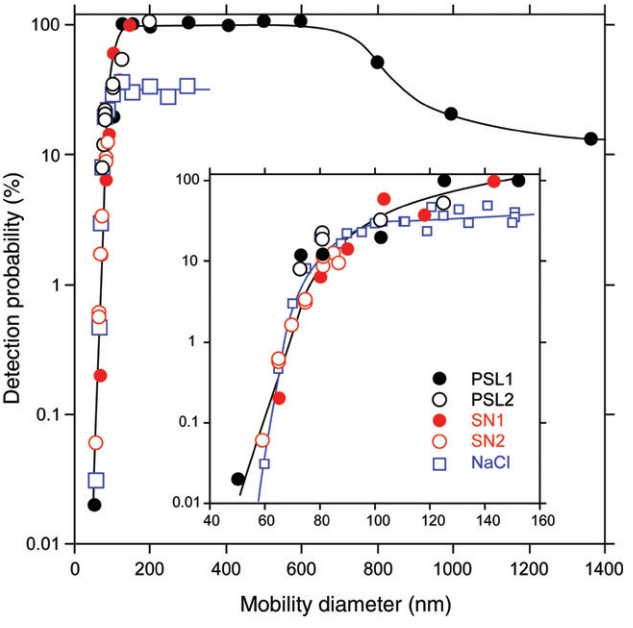

Figure 3. [Colour online] A plot of the detection efficiency of sodium nitrate, PSL and NaCl particles as a function of particle mobility diameter. The inset is a 'zoom in' view of ultrafine particles [16].

in particles' transmission efficiency of large particles through the aerodynamic lens inlet. The detection probability of smaller spherical particles decreases to 40% for 100-nm particles and to 1.5% for 70-nm particles. The fast decrease in detection efficiency of small particles reflects a rapid decrease in light scattering signal and a slight increase in particle beam divergence.

Thus far we have ignored the fact that aspherical particles form more divergent aerosol beams, which makes them harder to detect [9,12,44]. We quantified the effect of particle shape on the detection probabilities by using aspherical cubic NaCl particles and present the results in Figure 3, along with those of spherical particles, discussed above. The figure shows a detection efficiency of 30% for the larger aspherical particles and detection probabilities that are virtually indistinguishable from those of spherical particles for particles that are smaller than 100 nm.

In SPLAT II we make use of the differences between spherical and aspherical particle detection probabilities by continuously monitoring and recording the detection rates in the two optical detection stages. Since this ratio is a direct measure of the particle beam divergence, it provides real-time information about particle asphericity.

The observed detection probabilities for particles smaller than 150 nm are significantly higher than any other existing SPMS. At present, SPLAT II detects and characterises at least 1 particle per second, if the concentration of spherical particles that are between 125 and 600 nm in diameter are as low as 1 particle per cm^3. The significant increase in instrument sensitivity yields high sampling rates that are being taken advantage of by sizing up to 2000 particles per second and recording up to 100 IPMS per second.

To cover the wide range of particle compositions found in many fields requires a complex and flexible ion formation approach. In atmospheric science alone particle compositions include fragile organic molecules mixed with soot, dust and inorganic compounds like sulphates, nitrates and other acids and salts. Most laser-based SPMSs rely on ablation to generate ions for mass spectral analysis [39,45,46]. As a result the mass spectra generated by this highly non-linear, multi-photon process are strongly influenced by matrix effects and charge-transfer processes [47–50]. Consequently, it is not uncommon to find that the ablation generated mass spectra of atmospheric particles are dominated by a high abundance of K^+ or Na^+ ion peaks, the lowest ionisation potential species in the particle. The non-linearity of laser ablation also causes large particle-to-particle fluctuations in mass spectral peak intensities, hampering identification and quantification of particle mass spectra. Moreover, laser ablation-based mass spectra exhibit extensive fragmentation of the fragile organic molecules, often to the point where they cannot be distinguished from elemental carbon. In-short, ablation often leads to irreproducible, difficult to interpret mass spectra and general deterioration of quantitative capabilities of the SMPSs.

In contrast laser ionisation of molecules in the gas phase was shown to yield reproducible, high-quality and high-intensity mass spectra. For the semi-volatile compounds in particles it is possible to avoid particle ablation and instead generate ions by laser ionisation of gas phase molecules. To do so, the ion formation process is separated into two distinct sequential steps: particle evaporation with an IR laser pulse that is followed by time-delayed ionisation with a UV laser pulse. This two-step IR/UV approach has been demonstrated to greatly improve the analytical capability of SPMSs [12,51–55]. The SPLAT II uses a CO_2 laser to evaporate the semi-volatile fraction of the particle and a time-delayed ArF excimer laser at 193 nm to generate ions [16,55].

In Figures 4(a) and (b) we illustrate that, by controlling the spatial and temporal relationship between the IR and the UV laser pulses, it is possible to generate either a mass spectral signature that contains the semi-volatile fraction only or a mass spectrum of the entire particle. The figures show the results of a set of measurements [16,55] conducted on particles composed of a 139 nm non-volatile NaCl core coated with 59 nm of the semi-volatile dioctyl phthalate (DOP) to form 257 nm spherical particles with a NaCl weight fraction of 0.2 [25].

The spectrum in Figure 4(a) was generated by configuring the IR and UV lasers in such a way that the UV laser fires only after the particle centre-of-mass had passed by. At this point it ionises only the fraction of the evaporating DOP plume that expanded in the backwards direction. Not surprisingly, the spectrum in Figure 4(a) has only DOP peaks and no trace of NaCl is present. A simple examination of Figure 4(a) shows that, since the DOP mass spectrum exhibits significant intensity at $m/z = 149$ and 167, both of which are characteristic mass spectral peaks of phthalates, it is easily assignable. This mass spectrum is also clearly and unambiguously distinguishable from that of elemental carbon.

Figure 4(b) shows the mass spectrum of the same DOP-coated NaCl particles shown in Figure 4(a), except that this spectrum was generated by timing the UV laser pulse to hit the particle centre-of-mass. In this case both DOP and NaCl mass spectral signatures are present in the particle mass spectrum. The DOP fraction of the mass spectrum remains virtually unchanged, consistent with it being generated by gas phase ionisation. Since NaCl is not volatile, its mass spectral peaks were generated by ablation of the non-volatile

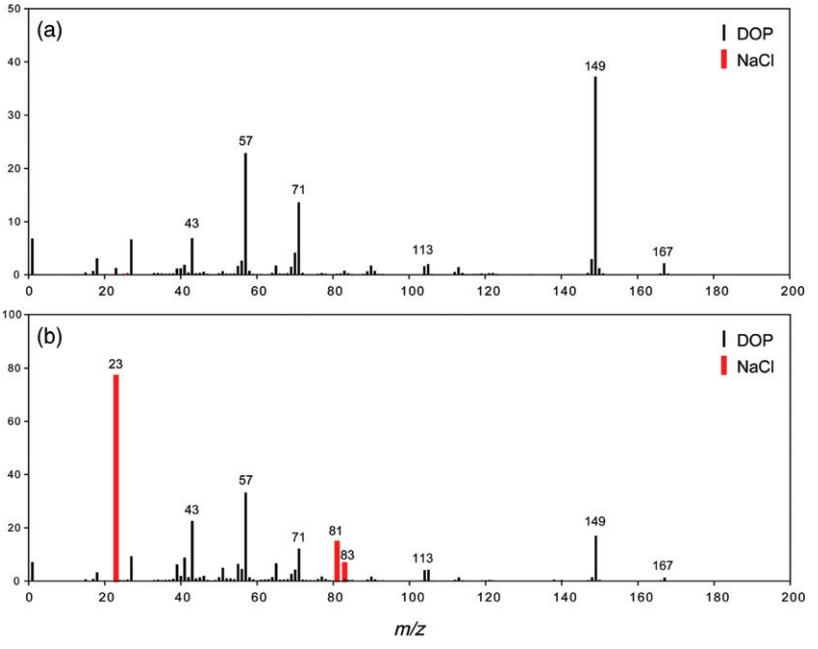

Figure 4. [Colour online] Average mass spectra of DOP coated NaCl particles, obtained in the IR/UV mode with the excimer laser delayed to miss the particle centre-of-mass (a) and hit the particle centre-of-mass (b) [16].

fraction of the particle. Here again we note that the two-step, IR/UV approach significantly diminishes the matrix effects and charge transfer processes that would have produced Na^+ dominated mass spectra.

This simple example illustrates the flexibility offered by this instrument to characterise either the complete particle composition or its semi-volatile fraction only. The mass spectra in Figures 4(a) and (b) demonstrate that the IR/UV, two-step ion formation approach significantly improves the data quality.

When SPMSs are deployed in the field to characterise ambient particles composed of a wide range of various internal mixtures they have to be operated at sufficiently high UV laser powers to assure good detection probabilities of *all* particle components, including those that are more difficult to ionise, of which sulphates represent the most commonly encountered example. At the higher laser powers that are required to ionise sulphate organic compounds tend to fragment to the point where their identification becomes virtually impossible.

Recently we have conducted a detailed comparative study between mass spectra of individual organic particles generated by UV laser ablation and in the two-step IR/UV mode [55]. Figures 5(a) and (b) present an illustrative example that compares the average mass spectrum of thousands of 334 nm DOP particles that were generated in the IR/UV mode (Figure 5a) to the one generated by UV laser ablation (Figure 5b). The UV laser fluence of 0.93 J/cm^2 used in this set of experiments was chosen to assure efficient ionisation of ammonium sulphate particles. Similar to the observations for the

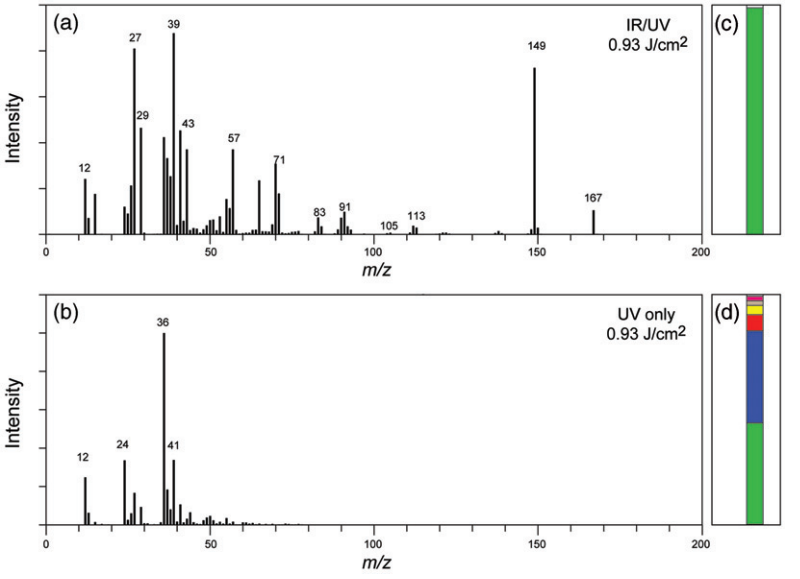

Figure 5. [Colour online] Average mass spectra of 334 nm particles composed of DOP obtained in the IR/UV mode (a) and by UV laser ablation (b). Bar graph representations of the classification results for the IR/UV mode (c) and for UV ablation (d) [16].

DOP-coated NaCl particles, the DOP mass spectrum in Figure 5(a) generated in the IR/UV mode exhibits significant intensity in the characteristic phthalate mass spectral peaks at $m/z = 149$ and $m/z = 167$. In contrast, the ablation-generated mass spectrum shown in Figure 5(b) exhibits a significant degree of fragmentation and has no intensity in these peaks, making it impossible to use it to recognise the presence of phthalate in these particles. As a matter of fact, the most intense peaks in this mass spectrum are those of C_1^+, C_2^+ and C_3^+, which are characteristic of elemental carbon or, soot particles.

A study of the dependence of mass spectral peak intensities on the UV laser power shows that while the IR/UV generated mass spectra are virtually UV laser power independent, the intensity pattern of ablation generated mass spectra strongly vary with the UV laser power [55].

An examination of the dependence of the integrated mass spectral peak intensities of mass spectra generated in the IR/UV mode on particle mass reveals a simple linear relationships that is observed for all the laser fluences used in this study. This relationship suggests the possibility to use mass spectral intensity to extract quantitative information on the basis of mass spectral data alone.

So far we have focused on the properties of the average mass spectra, but because the IPMS generated by SPMSs are classified *before* they can be averaged, it is critical to assess the instruments' performance by looking at the particle-to-particle mass spectral variability. Figures 5(c) and (d) are bar graph plots that show the results of the classification of mass spectra obtained in the two ion generation modes. Figure 5(c) shows that over 98% of the mass spectra generated in the IR/UV mode were classified into a single class, the average mass spectrum of which is shown in Figure 5(a). The bar graph

in Figure 5(d) illustrates the fact that the IPMS generated by laser ablation were classified into more than six separate classes, with the mass spectrum of the largest class being nearly the same as those of soot particles.

This simple example, which consisted of identical particles composed of a single organic compound, illustrates that ablation-generated mass spectra can produce a very complex picture of particle composition. Depending on the laser power and the classification routine we could be driven erroneously to conclude that a number of particle types were present and that a significant fraction of them were composed of soot. We clearly would have no mass spectral information that points to the presence of phthalates in these particles.

Both SPLAT and SPLAT II have participated in a number of field programs, located in Houston TX, New York NY, and Cheju Island (South Korea), Cummings Inc. (Columbus OH) and the National Transportation Research Center (Oak Ridge TN), where they were deployed to characterise ambient atmospheric particles and diesel exhaust particles. During the last field program SPLAT II was also deployed on an aircraft in a campaign designed to investigate the properties of ice clouds over the North Slope of Alaska. The analysis of the measured sizes and compositions of the millions of particles that were characterised during these field campaigns is not the subject of the present review. Here we focus on advancements that were made to improve data quality and extend instrument capabilities to measure, in addition to size and composition, other particles attributes.

The significantly improved instrument sensitivity translates directly to high temporal resolution, making it possible to obtain statistically robust data even on an aircraft. More importantly, high sensitivity is a key to being able to extend our measurement capabilities to include, in addition to size and composition, other particle properties like density, shape, fractal dimension and hygroscopicity. In the sections below we demonstrate that the relationships between particle mobility diameter and vacuum aerodynamic diameter can be used to extract many of these particle properties. Particle mobility diameter (d_m) is defined as the diameter of a sphere that has the same electrical mobility as the particle under consideration. DMA is typically used to measure d_m size distributions of particles, or to select particles with narrow distribution of d_m. Note that since the DMA selects and/or sizes only charged particles with a narrow size distribution it clearly results in a significant decrease in particle number concentrations. Consequently, to generate statistically robust datasets under these conditions calls for a very sensitive instrument.

3. Beyond size and composition: multidimensional characterisation of individual aerosol particles

We show above that SPLAT yields information on individual particle composition using the IR/UV ion generation approach and measures the vacuum aerodynamic diameter of each particle with an accuracy of 0.5% or better. In the following sections we review the measurements of additional particle properties and, while the mass spectrometry aspect is not presented in each of the sections, it should be clear that for each particle, in addition to the described measurements, there is an associated mass spectrum.

3.1. *Particle density*

Particle density is an important, intrinsic physical property of aerosol particles. Particle densities are used to convert particle size distributions into mass loading, to model particle aerodynamic properties, and are often correlated with particle optical properties [56]. The monitoring changes in particle densities can also be used to follow aerosol transformations resulting from chemical reactions [57]. In the absence of composition measurements, it is often used to aid in particle identification [24,58,59]. And likewise, in the absence of direct density measurements, particle composition was used to deduce aerosol density [60,61]. Here we review our approach to simultaneously obtain both: particle density and mass spectra, which together provide the means to quantitatively calculate the composition of internally mixed ambient [24] and laboratory generated particles [25].

A number of methods have been developed and applied for measuring aerosol density in the laboratory and in the field, the vast majority of which yield average ensemble densities irrespective of particles compositions or sizes [19,57–59,62–71]. One of the more common approaches to obtain particle densities is to measure particle mobility and aerodynamic [58,66–70] or vacuum aerodynamic diameters [19,57,71–74]. When the mobility and aerodynamic size distributions are measured in parallel, the calculated density is an average of the ensemble of particles and is calculated under the assumption that particle density is size independent. Size resolved density can only be obtained by measuring aerodynamic diameters of DMA-classified particles [17,19,24,73,75]. This approach most often reveals the particles to be composed of rich and complex mixtures, each with its distinct size distribution. Size resolved density has also been measured by combining the DMA to classify a narrow size distribution of particles and using an aerosol particle mass (APM) analyser [59] to measure their masses. The mobility diameter is used to calculate particle volume, which, together with the mass, yield particle density. This method, however, is not supplemented by information on particle composition.

Murphy *et al.* [65] applied their SPMS to measure mass spectra and densities of individual particles. In this technique an estimated individual particle density was obtained on the basis of the combined measurements of individual particle optical diameter and its vacuum aerodynamic diameter.

It is important to keep in mind that, in each of the approaches presented thus far, particles were either spherical or were assumed to be spherical. We will return to this issue in the sections where we discuss measurements of particle shape.

Our goal was to add to the measurements of individual particle size and composition a high precision measurement of its density. To this end we use a DMA to classify particles with a narrow distribution of mobility diameters (d_m), which is transmitted to SPLAT, where individual particle vacuum aerodynamic diameters (d_{va}) and mass spectra are measured. For a spherical particle the mobility diameter is equal to its physical diameter (d_p) and volume equivalent diameter (d_{ve}), and its density can be calculated according to Equation (1) from the measured (d_m) and (d_{va}) [19,71]:

$$\rho_p = \frac{d_{va}}{d_m}\rho_0, \tag{1}$$

where ρ_p and ρ_0 are the particle material density and unit density, respectively.

Since the calibration of SPLAT and the DMA remain extremely stable over the duration of typical experiments, the precision of the density measurements is at present

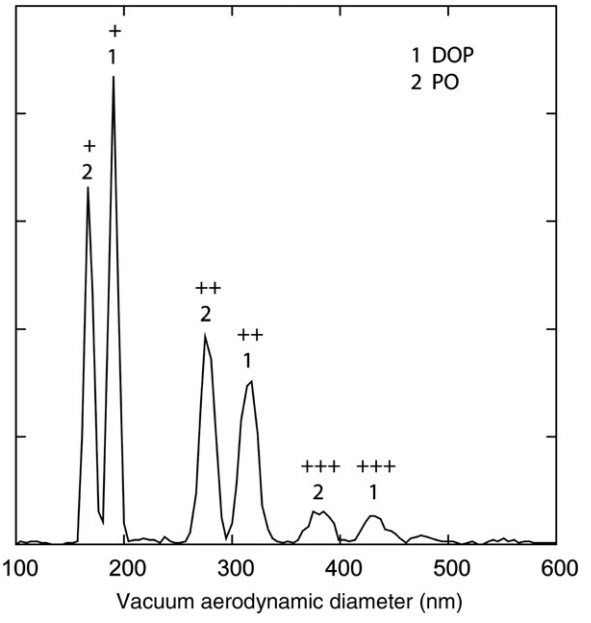

Figure 6. Measured vacuum aerodynamic diameters of DOP and PO particles classified by the DMA at 200 nm. The symbols '+, ++, +++' denote particle charge [19].

determined by the resolving power of the DMA, which is related to its operating conditions. Under normal conditions the DMA classified particle population has a distribution with a FWHM of 5%; however, we have demonstrated that the very same instrument can also be used to yield FWHM of $<2\%$. The accuracy of the measurements is directly related to the calibration of the combined SPLAT/DMA system. To carry out high-precision density measurements a calibrant aerosol of known density, like DOP, is typically used to simultaneously calibrate both instruments. Figure 6 provides an illustrative example of high-precision density measurement, in which DOP with density of $\rho_p = 0.986\,\mathrm{g/cm^3}$ was used as an internal calibrant to measure the density of particles composed of pump oil (PO). The DMA in this experiment was set to select particles with $d_m = 200\,\mathrm{nm}$, but a series of pairs of peaks is clearly visible. These peaks correspond to the multiple charged DOP and PO particles with the same electrical mobility, but different d_{ve} and d_{va}. The DOP and PO peaks are easily resolved despite the fact that their densities differ by only 14%. Averaged over all sizes we find the PO density measured by this scheme to be $\rho_p = 0.8664 \pm 0.006\,\mathrm{g/cm^3}$, which is within the uncertainty of the known PO bulk density of $\rho_p = 0.866\,\mathrm{g/cm^3}$. We demonstrated that using this approach we can perform density measurements with an accuracy of $\pm 0.5\%$ [19,75] and applied the developed method to a number of systems of interest [19,75–77].

Below we provide an example of the use of this approach to measure the density of particles of atmospheric importance in highly metastable phases.

Many atmospheric aerosol particles are hygroscopic. Their interaction with the atmospheric water vapour alters their size, density, phase and optical properties. In turn these physical properties directly impact aerosol role in climate change, visibility and even

Table 1. Extrapolated and observed densities for metastable phases and bulk crystal densities [19].

System	[56][a] (g/cm^3)	Observed (g/cm^3)	Crystal (g/cm^3)	Δ^b%
$Ca(NO_3)_2$	–	2.16 ± 0.02	2.54	15
$NaHSO_4$	2.22	2.19 ± 0.02	2.43	9
$NaNO_3$	2.09	2.10 ± 0.01	2.26	7
NH_4HSO_4	1.74	1.77 ± 0.02	1.79	1
NH_4NO_3	–	1.57 ± 0.025	1.73	8

Notes: [a]Extrapolated for 100 wt% solution droplets.
[b]% $\Delta = 100$ (Crystal − Observed)/Crystal.

public health. Thermodynamically, hygroscopic substances are expected to be crystalline at RH below the deliquescence point and solution droplets at RHs above the deliquescence point. However, small particles often depart from equilibrium thermodynamics and instead exist in supersaturated metastable states. How deep the supersaturation needs to be for crystallisation to occur depends on particle size and composition. In some 'extreme' cases, once solution droplets form it is virtually impossible to transform them back to the crystalline phase, even when the particles are in vacuum and the RH is clearly reduced to nearly zero. A number of systems of atmospheric significance belong to this class, among them are ammonium bisulphate [78], ammonium nitrate [79–83], sodium bisulphate [56], calcium nitrate [84] and sodium nitrate [23,47,85]. These particles form instead a 'glassy' amorphous phase that continuously absorbs and loses water in response to increasing or decreasing RH. While in some cases crystallisation can be induced by the introduction of nucleation centres, some of these particles were shown to remain in a 'glassy' metastable phase even when placed on substrates, or contain solid inclusions like a PSL particle [47].

Since the densities of these metastable phases are expected to be within ~10% of the crystal densities high precision is essential here. We took advantage of the high precision of the SPLAT/DMA system to measure the densities of several particle systems in deep metastable states, including calcium nitrate, sodium bisulphate, sodium nitrate, ammonium bisulphate and ammonium nitrate. The results of these measurements are summarised in Table 1.

We found that the densities of these hygroscopic particles in highly metastable 'anhydrous' droplet phases are 7%–10% lower than their crystalline densities, with the exception of ammonium bisulphate, for which the two phases differ by only 1% [19]. Where possible we used existing experimental data on the relationship between particle density and composition [56] to calculate densities for the 'anhydrous' solution droplets by extrapolating the data to 0 RH. For these cases good agreements between calculated and observed densities were found.

The amorphous calcium nitrate measured density was 2.16 ± 0.02 g/cm^3, which is 15% lower than the density of the anhydrous crystalline calcium nitrate of 2.54 g/cm^3 and significantly higher than the densities of two known α and β crystalline phases of the commercially available calcium nitrate tetrahydrate of 1.896 and 1.82 g/cm^3, respectively. The density we measured appears to be consistent with that of amorphous calcium nitrate with the formula $Ca(NO_3)_2 \cdot nH_2O$, where n is between 1 and 2, which is in good agreement with the results of the hydration–dehydration study of single suspended $Ca(NO_3)_2$ microparticles [84].

3.2. *Particle dynamic shape factor*

It is well known that a significant fraction of aerosol particles are aspherical, yet particles are routinely assumed to be spherical to enable an interpretation of many of the measurements of particle properties. The wide use of this assumption reflects the difficulty in experimentally determining particle true shape.

Particle shape and morphology have an indisputably important impact on particle properties, behaviour, chemical reactivity and consequently on the physical meaning of the measured attributes. For example, particle volumes are most often obtained by measuring particle mobility size distributions and under the assumption that the particles are spherical. These volumes are then converted to mass loads by using particle densities that are calculated from the measured mobility and vacuum aerodynamic diameters assuming again that the particles are spherical. Depending on the system, these assumptions can introduce significant errors. To set the scale that an assumption of particle sphericity can introduce, we will use an example from the study that investigated effect of shape on the mobility diameter of rod-shaped gold nanoparticles [86]. The authors showed that increase in temperature transforms these rod-like particles to nearly spherical. This shape transformation results in a decrease of particle mobility diameters from 55 to 25 nm. The assumption of sphericity for these rod-like particles leads to an overestimate of their volumes by more than a factor of 10. This simple example illustrates that these types of inaccuracies can play an important role in many aspects of aerosol science.

To account for the fact that the behaviour of an aspherical particle depends on its shape, a correction factor, called the dynamic shape factor (DSF), χ, is used. χ is defined as the ratio of the resistance force (typically the drag force) on the aspherical particle to the resistance force on a sphere of equivalent volume moving with the same velocity [87]. It is worth noting that the DSF is not an intrinsic particle property but a measure of its behaviour; it changes with pressure, particle size, and particle reorientation. In the present case d_m and d_{va} are measured at atmospheric pressure and in the vacuum, respectively. Based on the Knudsen numbers [88], *Kn*, the former is called the transition regime and the latter is the free-molecular regime. The relationship between the two observables we measure – d_{va} and d_m – and χ, the DSF, are given in Equations (2) and (3), respectively.

$$d_{va} = \frac{\rho_p d_{ve}}{\rho_0 \chi_v} \tag{2}$$

$$d_m = d_{ve} \chi_{t,\theta} \frac{C_c(d_m)}{C_c(d_{ve})}, \tag{3}$$

where ρ_p and ρ_0 are the particle material density and unit density, respectively, d_{ve} is particle volume equivalent diameter, χ_v is the DSF in the free-molecular regime in the random orientation, $\chi_{t,\theta}$ is an orientation-dependent DSF in the transition regime, and C_c is Cunningham Slip Correction Factor [88]. Since the Reynolds number in the aerodynamic lens inlet is smaller than ~0.03 [89], no particle alignment is expected [87] and the measured DSFs should be dominated by values for random orientation in free-molecular regime.

DeCarlo *et al*. [71] presented a theoretical exploration of the information content in simultaneous measurements of d_{va} and d_m, where they defined, for aspherical particles the so-called effective density ρ_{eff}. Analogous to the density of spherical particles, it is

based on the ratio of the two measured diameters as given in Equation (4), except that for aspherical particles the effective density depends on particle material density and on particle shape.

$$\rho_{\text{eff}} \equiv \frac{d_{va}}{d_m}\rho_0 = \frac{\rho_p}{\rho_0}\frac{1}{\chi_v \chi_{t,\theta}}\frac{C_c(d_{va}\chi_v\rho_0/\rho_p)}{C_c(d_m)} \tag{4}$$

Below we present the measurements made on several types of particle systems: starting with agglomerates of PSL spheres, used as a model system to develop a fundamental understanding of the information content in the measured quantities; and ending with particles of atmospheric relevance [17].

3.2.1. *The DSF of PSL agglomerates*

Polystyrene latex agglomerates are an ideal model system for the study of the effect of particle shape on particle behaviour. It is one of the few systems that can be reproducibly generated in the laboratory and for which shape, density and volume equivalent diameters are all precisely known. Figure 7 shows an example of the mobility size distribution of dried aerosolised suspension of 233 nm PSL spheres.

In addition to the singlets at 233 nm we observe peaks corresponding to doublets, triplets and quadruplets of PSL spheres. Also visible are peaks corresponding to multiply charged singlets and doublets as indicated in the figure. We carried out similar measurements using PSL spheres ranging in diameter from 51 to 404 nm. The observed mobility diameters were used to calculate the DSFs of PSL agglomerates in the transition regime using Equation (3) and Table 2 lists the calculated DSFs for the doublets only.

At first glance the data presented in Table 2 appear to indicate that the DSF is dependent on particle size. However, the corresponding changes in Knudsen number are too small to account for the observed changes in the DSFs. As the last column in Table 2 indicates, it is more likely that the observed differences in DSFs reflect changes in particle orientation in the electric field of the DMA [90,91].

Our data indicate that when PSL doublets are present in an electric field higher than 5000 V/cm, the induced dipole causes them to align parallel to the field. At lower electric fields (below 2000 V/cm) PSL doublets tend to be oriented at 45° to the field. Since lower voltage lessens the induced dipole, and smaller particles require higher voltage to induce a dipole moment, the two variables – lower voltage and smaller particles – work in consort to reorient particles from parallel to 45°. As the induced dipole moment diminishes, the dominant effect becomes aligned due to point charge, which results in 45° orientation. Note also, that the smallest doublets do not fully align even at highest electric fields, but are present instead in a nearly random orientation. In addition to the measured DSF values Table 2 provides comparison between our observed DSFs and those calculated on the basis of parameters given by Cheng *et al.* [90] and Kousaka *et al.* [91] for the parallel and 45° orientations, respectively. As the table shows, our measured DSFs are in excellent agreement with the calculated values. Similar results were obtained for compact triplets of PSL spheres, for which we also observed particle alignment in the electric field of the DMA. As for the case of doublets, our measured size-dependent DSFs for the compact triplets were found be in very good agreement with calculated values [17].

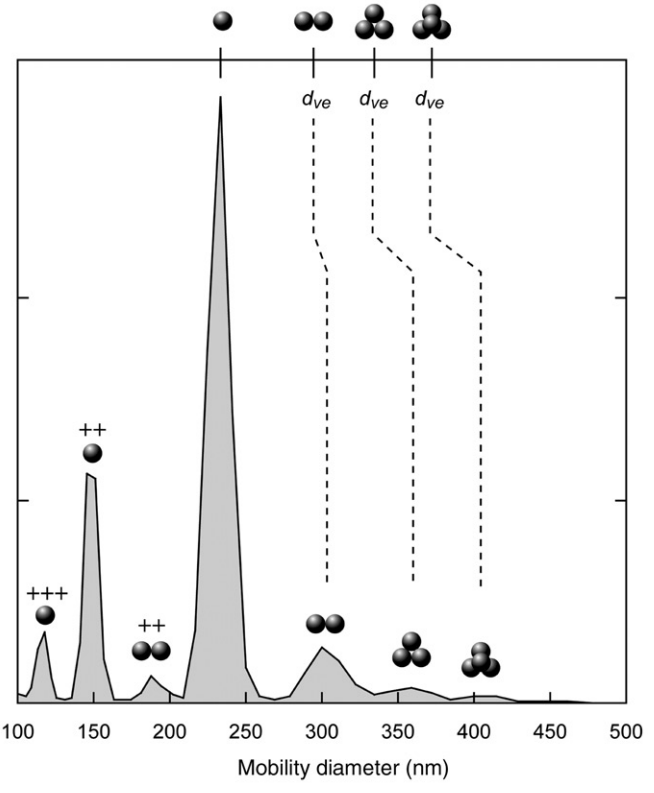

Figure 7. A mobility size distribution of aerosol produced by aerosolising and drying a suspension containing 233 nm PSL spheres. Apparent in the distribution are singlets, doublets, triplets and quadruplets. The peaks with mobility diameters smaller than the singlet correspond to multiply charged particles as marked. Also indicated are the volume equivalent diameters of the observed agglomerates. The upper scale provides the voltage in the DMA. To obtain electric field, a gap of 1.024 cm between the two electrodes should be used [17].

Table 2. Dynamic shape factors for doublets in the DMA [17].

Primary sphere size (nm)	Measured $\chi_{t,\theta}$	Literature χ	Orientation
50	1.10	–	45° – random[a]
73	1.07	1.08 [91]	45°
81	1.09	1.08 [91]	45°
125	1.08	1.08 [91]	45°
152	1.08	1.08 [91]	45°
199	1.05	1.01 [91]	Transition
204	1.03	–	Transition
233	1.03	–	Transition
299	1.01	–	Parallel
302	1.01	1.01 [90]	Parallel
350	1.02	1.01 [90]	Parallel
404	1.02	1.02 [90]	Parallel

[a]Appears to be between 45° and randomly oriented.

Table 3. Summary of the DSFs of PSL spheres agglomerates in the free–molecular regime and in the DMA [17].

d_1 (nm)	n	d_{ve} (nm)	d_{va} (nm)	d_m (nm)	χ_{vr}	$\chi_{t,\theta}$
204	1	204	214	204	1	1
	2	259	232	259	1.157	1.03
	3	294	253	310	1.213	1.082
	4	324	279	357	1.21	1.14
	4	324	273	376	1.24	1.205
	5	349	313	381	1.168	1.12
	7	390	331	449	1.24	1.20
	10	440	368	528	1.26	1.26
233	1	233	245	233	1	1
	2	294	269	303	1.147	1.034
	3	336	291	360	1.21	1.100
	4	370	319	408	1.215	1.14
	4	370	309	432	1.258	1.228
	6	423	364		1.22	
	7	446	394	527	1.189	1.19
	8	466	404	555	1.21	1.15
	10	502	440	622	1.20	1.21
302	1	302	317	302	1	1
	2	380.5	352	383	1.136	1.010
	3	435.5	379	465	1.207	1.089
	4	479	417	525	1.206	1.12
	5	516	464		1.167	
	8	604	532	670	1.19	1.15

While a number of experimental studies of PSL agglomerates have been conducted in the continuum and transition regimes [91–97], our study [17] was the first report on the experimental measurements of the DSFs of PSL agglomerates in the free-molecular regime. These measurements became possible by taking advantage of the DMA to isolate each of the agglomerates at a time and by the extremely high precision with which SPLAT sizes particles. Table 3 provides a list of the free-molecular regime DSFs for agglomerates of PSL spheres with three sizes (d_1). These values were calculated on the basis of the SPLAT measured d_{va} and the known d_{ve} using Equation (2). As the table shows, we were able to measure the DSF of significant number of agglomerates that ranged in complexity from doublets to agglomerates containing $n = 10$ PSL spheres. Nearly all the characterised agglomerates were unambiguously identified as compact in shape.

An example that illustrates the data quality is shown in a plot of the observed d_{va} distribution of the doublets of 233 nm PSL spheres obtained by setting the DMA to transmit into SPLAT particles with $d_m = 305$ nm as indicated by the arrow in the inset in Figure 8. Note that, despite the fact that the PSL suspension contained in addition to PSL doublets many other agglomerates, the only particles observed by SPLAT, in this scan, are the doublets. The simplicity and high signal to noise ratio of the doublets d_{va} distribution is a result of using the DMA as a filter and a testament of SPLAT's high sensitivity. The d_{va} distribution of the doublets peaks at 269 nm; taking into account the

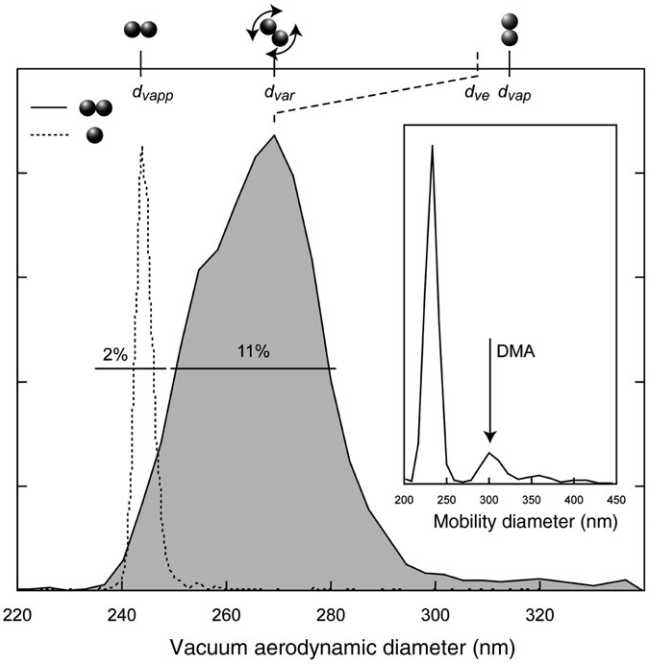

Figure 8. A comparison between the d_{va} distributions of the PSL doublets and singlets. The inset shows the DMA scan and the arrow points to the mobility diameter that was selected for the PSL doublets. The line widths (FWHM) for the two distributions are indicated. The top scale indicates the volume equivalent diameter and the calculated d_{va} of the doublets oriented parallel and perpendicular to the flow direction [17].

known d_{ve} of 293.6 nm and a density of 1.05 g/cm^3 we derive a DSF of 1.147 for the PSL doublets in the random orientation in the free-molecular regime.

A comparison between the size distributions of the PSL doublets and singlets in Figure 8 shows that the line shapes of the d_{va} distributions of these two particle types are significantly different and must also contain noteworthy information. The d_{va} distribution of the doublets exhibits a line shape with FWHM of 11%, which is significantly larger than the width of 3% expected purely on the basis of the line shape of the singlets. The increase in line width is directly related to the fact that the particle DSF depends on the particle orientation. In this case it is known that the DSFs of doublets in the parallel and perpendicular orientations are 0.98 and 1.25, respectively [90]. Translated to d_{va} for the 233 nm doublets we calculate vacuum aerodynamic diameters of 314.6 and 235 nm for the parallel and perpendicular orientations, respectively. These values set a scale for the upper and lower limits of the d_{va} distribution and are graphically noted in Figure 8.

To measure the DSFs of other agglomerates the DMA was successively tuned to the appropriate mobility diameters and the d_{va} distributions of the resultant aerosol were measured by SPLAT. By tuning the DMA and recording d_{va} distributions it was possible to measure the d_{va} and d_m and calculate DSFs for both regimes for a number of PSL agglomerates.

As noted above, we found perfect agreement between the calculated DSFs [92,98,99] for the doublets and those observed in our study [92,98,99]. Applying similar formulations that were developed for straight chains, to compact triplets and quadruplets was found to be somewhat less successful. A comparison between $\chi_{t,\theta}$ and χ_v reveals that alignment and pressure play an important role in determining the observed d_{va} and d_m. We also demonstrated that for the larger *compact* agglomerates, however, these effects seem to diminish and $\chi_{t,\theta} \approx \chi_v$.

On the basis of the data generated by SPLAT on the DSFs of PSL agglomerates in the free-molecular regime we also conclude that as a general rule, asphericity increases the width of the d_{va} distribution. We will return to this point later in the review.

3.2.2. *Dynamic shape factors of irregularly shaped particles*

In the section above we applied the SPLAT/DMA system to measure the DSFs of particles with known density and d_{ve} in two flow regimes. We found that the apparent differences between $\chi_{t,\theta}$ and χ_v reflect for the most part differences in orientation that are due to particle alignment in the DMA. In other words, as long as alignment in the DMA can be avoided, by operating at low electric fields, the simplifying approximation that $\chi_v = \chi_{t,\theta}$ is applicable. We define a new approximate DSF $\overline{\chi}, \chi = \chi_v = \chi_{t,\theta}$ and thereby make it possible to calculate *a* DSF ($\overline{\chi}$) using Equation (4) and measured particle d_{va} and d_m, for randomly shaped particles whose density is known.

Below we describe the study [17] that included the first experimental determination of the DSFs for several common particles of atmospheric importance. We illustrate the results with nearly spherical ammonium sulphate particles and cubic sodium chloride particles, both of which are not expected to be impacted by the effect of alignment in the DMA.

In this study [17] we performed the first *in situ* measurements of the DSF of ammonium sulphate particles, which is most often treated as if it is spherical. We measured simultaneously d_{va} and d_m for ammonium sulphate particles with a wide range of sizes, and calculated using Equation (4) the average DSFs for each particle size. We found that smaller ammonium sulphate particles are mildly aspherical with $\overline{\chi} = 1.03$ – consistent with their microscopic images and measured multi-angle light scattering signal [100,101]. However, one of the surprising findings from this study was that the ammonium sulphate DSF is size dependent. Our data indicated a systematic increase of the DSF from 1.03 to 1.07, as particle mobility diameter increases from 160 to 500 nm. The micrographs of ammonium sulphate particles that were acquired in parallel also show that larger particles have tendency to be more aspherical. An analysis of the observed line shapes shows that the precise DSF of ammonium sulphate particles depends on the way these particles are dried. It was not uncommon to find that two particle types, with slightly different shape factors, were present under some drying conditions.

Another example of aspherical particles of atmospheric importance – sodium chloride particles – are generally assumed to be cubic in shape with calculated DSF of 1.08 [87]. Our study [17] showed that when NaCl particles are generated by the most common method of aerosolising an aqueous solution of NaCl and drying the resulting aerosol flow, three types of NaCl particles were generated: (1) nearly spherical; (2) cubes and (3) agglomerates. Figures 9(a) and (b) summarise the NaCl data in plots of measured effective densities and calculated DSFs as a function of particle mobility diameter for the three particles types.

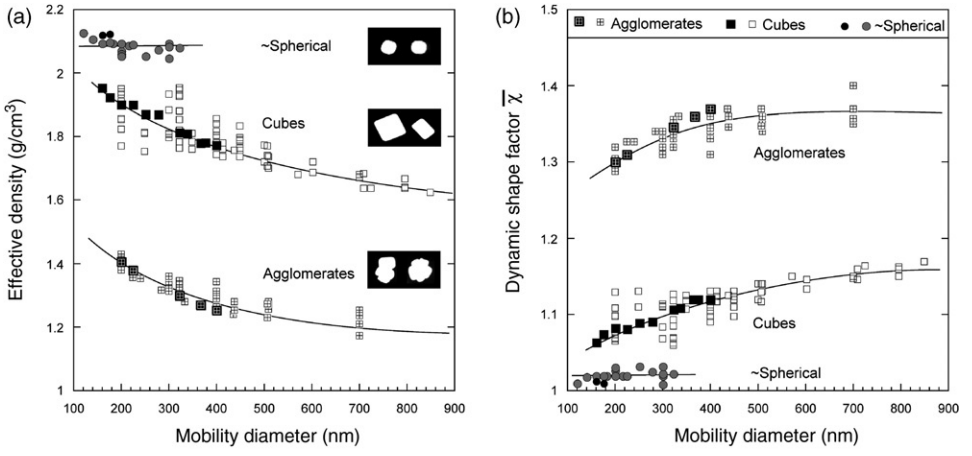

Figure 9. Size dependence of the derived effective densities (a) and DSFs (b) plotted as a function of sodium chloride particle mobility diameter. Three distinct types of sodium chloride particles are evident: nearly spherical, cubic and agglomerated. Micrographs of representative particles of each type are also shown [17].

The calculated DSF for the nearly spherical NaCl particles was found to be 1.02 ± 0.01 independent of particle size. Note, however, that this particle type was observed only for the particles with smaller mobility diameters (< 322 nm).

The cubic form of NaCl was the most prevalent. The calculated DSF for this form of NaCl particles is size dependent, increasing from 1.06 to 1.17 as particle size increases from 200 nm to 800 nm. The DSF smaller than 1.08 indicates the presence of cubic particles with rounded edges and DSF larger than 1.08 is consistent with rectangular particles.

The larger spread in the calculated DSFs observed for smaller particles reflects true run-to-run variability in particle shape due to small changes in particle generation and drying conditions. An example that represents data acquired in a single run is illustrated in Figure 9 with the filled squares data points. It shows a simple smooth trend with very little spread.

In addition to the two particle shapes described above we observed NaCl particles with very low effective densities and hence large DSFs. These were NaCl agglomerates that typically form by coagulation of smaller particles at high number concentrations. The micrograph shown in the inset in Figure 9(a) and many others like it are consistent with relatively compact irregularly shaped agglomerates with primary particle sizes ranging from 50 to 100 nm. Our calculated DSFs for this form of NaCl are 1.3–1.4, consistent with the DSFs for large compact PSL agglomerates presented in the previous section. Highly irregular chain-like NaCl agglomerates formed by condensation, with DSFs up to 5, were previously observed in several studies [102]. Following humidity induced micro rearrangements these agglomerates were shown to become compact with DSFs below 1.5, which are consistent with the DSFs we observe for this NaCl particle form.

Even when material density is not available, the particle effective density is a good measure of particle properties. We demonstrated that under carefully reproduced

conditions the effective density and particle mass spectral data comprise a signature for a particle identification scheme and can be used to extract quantitative information on the internal compositions of individual particles [24,25]. Accordingly, effective density can be used to improve data classification and visualisation process.

3.3. *The properties of diesel exhaust particles and particle fractal dimension*

Diesel exhaust particles play major roles in impacting the global climate and human health. There is no question that reliable climate modelling must include proper representation of these particles. A similar statement can be made with regards to air quality modelling, particularly in urban areas.

We have had the opportunity to deploy SPLAT to characterise the properties of diesel exhaust particles under a wide range of engine operating conditions and fuel types. Nearly 0.5 million particles were characterised, producing vast amount of detailed information. Here we provide only a very brief description of the salient findings.

Our data show that exhaust particles are internally and externally mixed and that each particle type can be found in a range of compositions. In Figure 10, we show an example of mass spectra of four individual particles that are commonly found in diesel exhaust. Figure 10(a) shows a spectrum of a 49 nm soot particle. Under normal engine operating

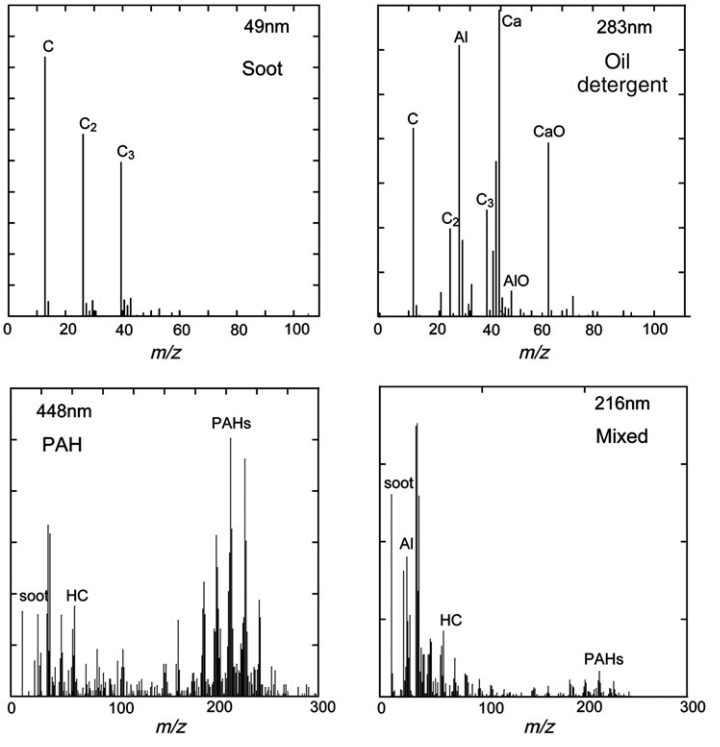

Figure 10. Four mass spectra of individual exhaust particles [12].

conditions soot represents the most common particle type. A careful analysis of the mass spectral data shows that most often soot particles do contain a very small amount of polyaromatic hydrocarbons (PAHs) and a few other complex organics. We will return to these particles below.

Figure 10(b) is of a 283 nm particle containing Ca, Al, unburned fuel and soot. Particles composed of calcium phosphate, used as an oil detergent, Al and a little bit of soot are often present in diesel exhaust. They are indicative of high oil consumption and engine wear and tear and become more prevalent under low load and high RPM conditions. These particles have vacuum aerodynamic diameters that are significantly larger than those of pure soot particles. The average effective density of these particles is $\sim 2\,g/cm^3$, consistent with their large metal and mineral content.

Figure 10(c) is an unusually large PAH particle. Most PAH dominated particles are internally mixed with unburned fuel and a small amount of soot. Since they come in a wide range of compositions their effective densities exhibit relatively wide range. Similar to the previous particle type, PAH particles are more prevalent under low load and high RPM conditions.

Figure 10(d) is a 216 nm internally mixed particle composed of nearly each of the substances present in the other three particles.

Freshly emitted soot particles are composed of agglomerates of much smaller ($\sim$10–30 nm) primary spherules [71,103–105]. Their complex 3-D structures are often fractal, with fractal dimensions that are related to their formation mechanisms.

Equation (5) provides an approximate relationship between the effective density of soot particles and their fractal dimension [71]:

$$\rho_{\text{eff}} \equiv \frac{d_{va}}{d_m}\rho_0 = C d_m^{D_f} f^{-3}. \tag{5}$$

Here C is a constant and D_f is the fractal dimension. For spherical particles $D_f = 3$, for compact agglomerates $D_f \approx 3$, long straight chains have $D_f \approx 1$. Note that for a $D_f = 2$, d_{va} must be constant.

Equation (5) shows the measurement of particle effective density that can be used to gain information about the fractal structure of soot particles in this exhaust. To this end, we have conducted, in addition to the traditional measurements of particle size and composition, a set of experiments, in which a DMA was used to classify the particles with a number of mobility diameters, before they were sampled by SPLAT. Combining particle mobility diameter with the measured d_{va} yields particle effective densities [21]. In the present case the IPMS were used to classify and organise the data into classes representing particle compositions. The data for soot particles were then isolated and the relationship between their observed effective densities and mobility diameters was examined. Figure 11 shows the results of applying this approach to data obtained from two different engines.

According to Equation (5) the data presented in Figure 11 can be used to estimate the fractal dimensions of the soot particles. The linear fits to the data in Figure 11 yield fractal dimension of 1.87 and 1.97 for the two diesel engines as indicated on the figure. Both of these values are consistent with the theoretically predicted value of 1.90 ± 0.07 [106] for soot that is formed by diffusion-limited cluster–cluster agglomeration.

As noted above, the vacuum aerodynamic diameter of particles whose fractal dimension is 2 is constant. Our data show that the soot particles characterised in this

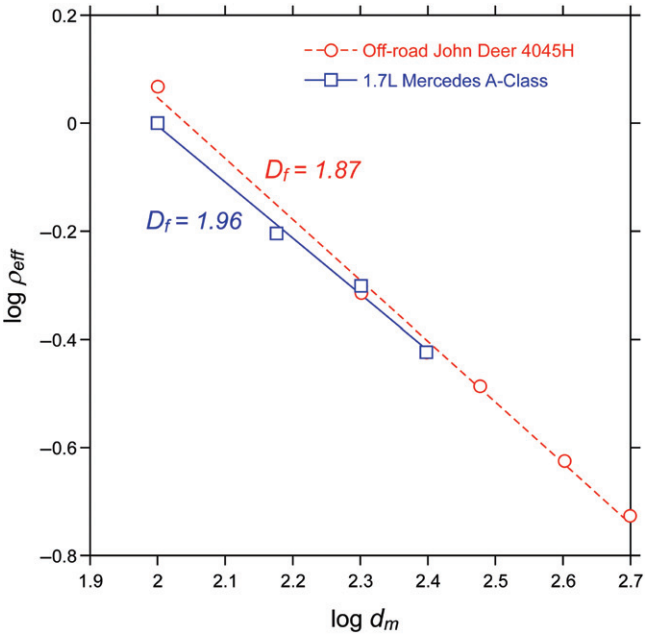

Figure 11. [Colour online] The measurements of effective density of soot particles as function of their size [21].

study have an average vacuum aerodynamic diameter that is very close to 100 nm and is nearly independent on soot mobility diameters.

3.4. *Particle asphericity*

There are many conditions under which confirming that the particles are spherical, or for that matter knowing that they are not, can greatly enhance our understanding of the aerosol system and aid in data interpretation. Particle asphericity has commonly been detected using light scattering [100,101]. In remote sensing, high laser depolarisation ratios are used to indicate the presence of aspherical particles. Angle-resolved light scattering has been successfully used to determine particle sphericity during *in situ* sampling. A more recent method is based on measuring the divergence of a particle beam formed by an aerodynamic lens inlet, such as the one used in SPLAT [44,57,107]. A number of studies have shown that the particle beam divergence is strongly dependent on particle shape, with spherical particles forming particle beams that are narrower and have significantly lower divergence than those formed by aspherical particles [9,12,16,18,40,41,57,108]. Hence, by quantifying the particle beam divergence, it is possible to distinguish between spherical and aspherical particles [44,107].

In Figure 8 we have already shown that there is a clear difference between the line shape of the d_{va} distributions of the aspherical PSL doublets and that of the spherical PSL singlets. We pointed out that the observed line broadening, for aspherical particles, reflects the orientation dependence of their DSF [17,19]. It is important to recognise that the

discovery of line broadening phenomenon became possible in part because of a uniquely well-defined narrow d_{ve} distribution of PSL spheres and their agglomerates. Extension of this approach to other randomly shaped particle types, including ambient aerosols, requires the use of a DMA to select particles with a narrow and well-defined mobility size distribution. The selected particle population is transmitted to SPLAT, where their d_{va} distributions are measured. Note that, without the high sizing resolution offered by the SPLAT/DMA system, it would be impossible to unambiguously establish the fact that particle asphericity causes broadening of the d_{va} distributions [17,19,75]. Moreover, as we described above, the very same measurements are used to determine, with high precision particle densities, effective densities, DSF and particle compositions.

In Figure 12 we demonstrate the capability to distinguish between spherical and aspherical particles on the basis of the line shape of their d_{va} distributions using cubic NaCl particles, pyrene-coated NaCl particles, and DOP-coated NaCl particles. Figure 12 shows, superimposed, the measured d_{va} distributions of the three, DMA selected, particle types.

The NaCl particles are classified by the DMA at 146 nm and their measured vacuum aerodynamic diameter peaks at 270 nm. The line shape in Figure 12 for these particles is broad and asymmetric with a FWHM of 10%. The calculated effective density of these particles is 1.85 g/cm^3, which together with the known NaCl material density of 2.165 g/cm^3 yields, according to Equations (4) and (5), a DSF of 1.08. This DSF is in perfect agreement with previously reported values of cubic particles [17,87,96].

When the very same NaCl particles, with $d_m = 146$ nm are coated with DOP, a liquid organic substance, the line shape, shown in green in Figure 12, narrows down to FWHM of 5%. This line width is consistent with the value observed for a wide range of spherical particles, when classified by a DMA that was operated under identical conditions.

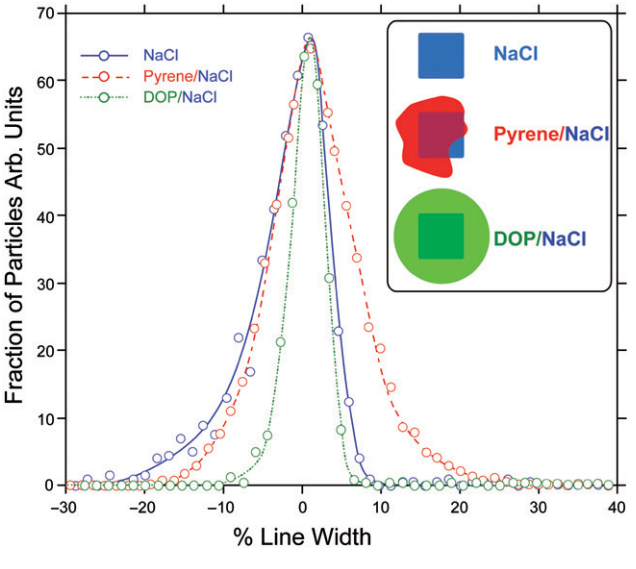

Figure 12. [Colour online] Line shapes of d_{va} distributions of DMA classified: cubic NaCl particles, NaCl particles coated with solid pyrene and NaCl particles coated with liquid DOP [20].

This simple observation provides unequivocal evidence that the DOP coating transformed the cubic NaCl particles into spherical particles.

Since we have now established on the basis of the d_{va} line shape that the DOP-coated NaCl particles are spherical, we know that their $d_m = d_{ve} = 257$ nm. We also know that the NaCl core has $d_m = 146$ nm and based on its calculated DSF of 1.08 we compute that its $d_{ve} = 139$ nm. This information is used to calculate a NaCl volume fraction of 15.9% for these DOP-coated NaCl particles. Furthermore, the known densities of NaCl and DOP, and the calculated volume fractions can be used to calculate a particle density of 1.17 g/cm^3 for these particles. This value is in very good agreement with our measured density of 1.164 ± 0.01 g/cm^3. The excellent agreement between the calculated and the measured densities provides further support for our conclusion that these particles are spherical and the precision with which these measurements can be carried out.

In contrast with the DOP-coated NaCl particles, the line shape of the pyrene-coated NaCl particles, shown in red in Figure 12, exhibits a line width of 13%, slightly larger than that of the NaCl core particles. This observed line width clearly indicates that the pyrene-coated particles are not spherical. Given that pyrene is a solid, this finding is not surprising.

The pyrene-coated NaCl particles were classified at $d_m = 241$ nm and their measured $d_{va} = 272$ nm, which together yield an effective density of 1.13 g/cm^3. The fact that the effective density of these particles is smaller than the density of either of the two particle constituents (1.271 g/cm^3 for pyrene and 2.165 g/cm^3 for NaCl) provides additional, unambiguous support for the conclusion that these particles are aspherical. Using the measured effective density of 1.13 g/cm^3, the calculated d_{ve} of the NaCl cores, and the known material densities of NaCl and pyrene, we determine that these pyrene-coated NaCl particles have DSF = 1.155; $d_{ve} = 218.6$ nm; and a pyrene weight fraction of 63.0%. Note that in this case the assumption of particle sphericity would have resulted in an overestimation of the particle volume by 36%, and the effective density would be unphysical.

It is worth noting that these findings regarding the morphologies of coated NaCl particles were confirmed by conducting a 'depth-profiling' study of the very same particles [25], which will be described in Section 3.5.

These few simple examples provide strong evidence for the existence of a robust relationship between the particle shape and the width of the d_{va} distribution of particles with narrow mobility size distributions. We have tested this relationship on a significant number of systems and find it to be very reproducible [17,19,25].

This approach was also applied to characterise the properties of secondary organic aerosol (SOA) [75,76]. We found that SOA particles formed by homogeneous nucleation during ozonolysis of α-pinene with and without an OH scavenger are spherical and that their densities are 1.213 ± 0.003 g/cm^3 and 1.198 ± 0.004 g/cm^3, respectively. These results represent the first direct high-precision density measurements and unambiguous shape determination of SOA particles [75].

3.5. *Particle asymmetry*

In Section 3.2.1 we already discussed the effect of particle alignment in the electric field of the DMA on particle DSF, and by extension on the observed mobility diameters of

aspherical particles [17]. We have clearly established that because of alignment effects the mobility diameters of aspherical particles can depend on the electric field at which they are measured. In contrast, the mobility diameter of spherical particles is electric field independent. On that basis we developed a novel approach to distinguish between particles on the basis of their asymmetry [18]. In this approach we deploy a tandem of DMAs (TDMA) in a manner designed to reveal the relationship between the particle mobility diameter and the DMA electric field. Here we rely on the relationship between the sheath flow rate and the electric field at which particles of specific mobility are classified – the higher the flow rate, the higher is the electric field. In this system the first DMA, operated with a high sheath flow rate is used to select particles with a narrow distribution of d_m, which are then sampled by the second DMA in which the sheath flow rate is varied and the particle mobility diameter is measured as a function of electric field. The finding that the mobility diameter varies with electric field provides unequivocal evidence that the particles are aspherical and asymmetric.

As we have done previously, we started this study by testing our approach on PSL agglomerates, for which shapes, volume equivalent diameter, as well as the orientation dependence of the DSF are all known. The results of these experiments demonstrated that asymmetric PSL agglomerates align parallel to the electric field at high electric fields and approach random orientation at significantly reduced electric fields. We also established that, since the DSFs are at a minimum in the parallel orientation, the mobility diameters are the smallest at the high electric fields. As the electric field is decreased asymmetric particles reorient towards the random orientation, their DSFs increase and so do their mobility diameters.

We found that the electric fields at which particles change orientation are a function of particle shape and particle size. Our data clearly showed that the alignment behaviour of PSL doublets with up to four charges is independent of particle charge, indicating that the induced dipole moments dominate the forces that determine particle orientation and that point charge interactions are less important. This finding also explains the observed fact that smaller particles require higher electric field to be aligned in the parallel orientation. We showed, for example, that doublets of PSL spheres with diameters of 129 nm and smaller require fields that exceed the maximum field available for typical DMA (10 kV/cm) to align in the parallel orientation. In contrast, doublets of PSL spheres with diameters of 200 nm or larger align in the parallel orientation at electric fields of ~5000 V/cm and higher. The data also suggest that the electric field at which particles reorient is closely related to the particles' longest dimension: the larger the longest dimension is, the lower is the required electric field, to achieve parallel orientation.

The extension of this method to a variety of symmetric and asymmetric particles with different shapes and aspect ratios revealed that particles with larger aspect ratios, like thin graphite 'flakes' and ellipsoidal hematite particles have larger DSFs and exhibit greater differences in DSFs as a function of reorientations and thus larger changes in d_m with changes in electric field. The particle systems we investigated in this study have DSFs that range from 1 to ~1.5.

An overview of the results shows that the mobility diameters of the asymmetric particles were found to increase by nearly 10%, while their DSFs increased by as much as 15% as they reorient from parallel to nearly the random orientation.

We showed that the measurements of changes in particle d_m as a function of the DMA electric field provide insightful information about particle shape and symmetry, but alone they are insufficient to derive the particle DSF. As noted above, the combined measurements of the d_m and the SPLAT-measured d_{va}, on the other hand, can be used to calculate an approximate DSF ($\overline{\chi}$) for particles of known densities. We demonstrated that when calculating $\overline{\chi}$ for particles that exhibit alignment effects in the DMA it is advantageous to use the d_m measured at the lowest electric field. This approach minimises the effect of alignment in the DMA, making the two measurements, in the transition and the free-molecular regime, under similar orientation, thereby giving a clearer meaning to the calculated DSF with respect to particle orientation.

Our observations of changes in mobility diameter as a function of electric field for nine types of particles used in this study [18] allowed us to distinguish between particles on the basis of their shape and symmetry, and were found to be in perfect agreement with the results of microscopic image analysis. Measurements of cubic NaCl particles ($\overline{\chi} = 1.10$), nearly spherical ammonium sulphate ($\overline{\chi} = 1.05$), and the pseudocubic form of hematite particles ($\overline{\chi} = 1.05$–1.10), all indicated that these particles are aspherical, and that they have either special symmetry, or that their asymmetries are too small to orient in the electric field.

Measurements of thin graphite 'flakes' ($\overline{\chi} = 1.5 \pm 0.2$), ellipsoidal hematite particles with aspect ratios of ~2.5 ($\overline{\chi} = 1.27 \pm 0.02$) and ~3.25, doublets and triplets of PSL spheres and agglomerates of aluminium oxide nanoparticles have all indicated that these particles are aspherical, asymmetric and their aspect ratios and longest dimensions are sufficiently large to orient parallel in the DMA at high electric fields.

Figures 13(a) and (b) provide an illustrative example of some of the options that this approach offers. Figure 13(a) shows the results of a set of two measurements conducted on a sample of hematite particles that happened to contain particles of two

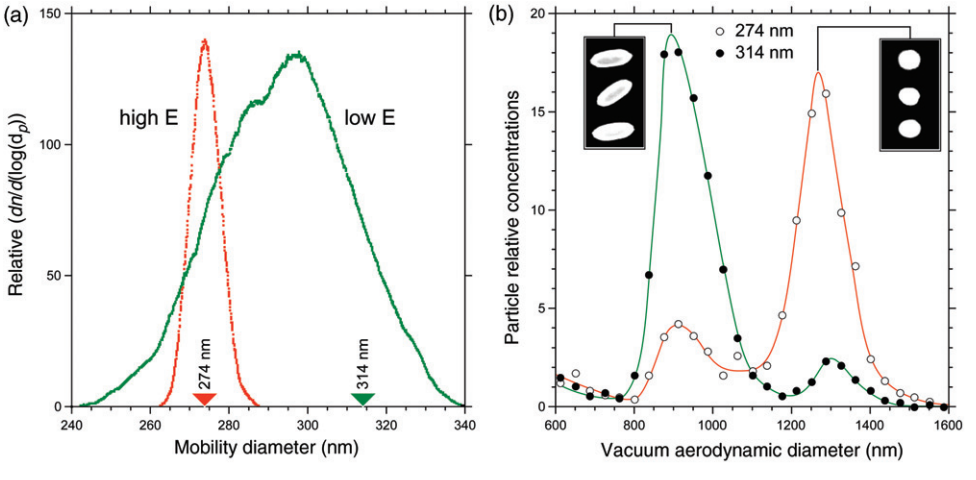

Figure 13. [Colour online] (a) Two mobility size distributions of 274 nm hematite particles obtained by the second DMA at high and low electric field (E), as indicated; (b) d_{va} distributions of 274 nm Lot 32 particles selected by the second DMA low electric field, to have mobility diameters of either 274 nm or 314 nm. The micrographs show the two particle types [18].

different shapes: the majority of the particles were ellipsoidal with aspect ratios of ~2.5 and a small fraction of particles were nearly spherical. The first DMA that was operated under high electric field conditions classified this mixture of particles at 274 nm. When the second DMA was operated at the same high electric field conditions as the first one, the observed d_m distribution peaked at the selected $d_m = 274$ nm and its line shape remained narrow (red trace in Figure 13(a)). A second scan of the second DMA was carried out at much lower sheath flow rate and, hence, electric fields and its results are shown with the green trace in Figure 13(a). The figure clearly shows that the new mobility size distribution is shifted from 274 to 296 nm and that it became much broader.

The presence of two very different particle types, both of which were selected by the first DMA that was set to select particles with $d_m = 274$ nm, was first revealed by the measurements of the d_{va} distribution of the particles from this lot. One particle type had a d_{va} of 920 nm and the second had a d_{va} of 1266 nm. Given that the two particle types had identical d_m at high electric field and identical composition, the large difference in their d_{va} suggested that they must have significantly different particle shapes. This finding was later confirmed by the examination of these particles' micrographs. Consequently we assigned the peak with $d_{va} = 920$ nm to the ellipsoidal particles and the second peak at $d_{va} = 1266$ nm to the nearly spherical particles.

Because these particles have very different shapes, their mobility diameters are expected to behave very differently as a function of the electric field in the DMA: while the mobility diameters of the nearly spherical particles should be independent of the electric field, the mobility diameters of the ellipsoidal particles is expected to shift to larger mobility diameters with decreasing electrical field in the second DMA. To test this hypothesis we operated the second DMA at the settings corresponding to the low electric field and set it to select particles with either $d_m = 274$ or $d_m = 314$ nm (both values are marked in Figure 13(a)). The d_{va} distributions of the particles selected by the second DMA were measured by SPLAT and the results of these two measurements are presented in Figure 13(b). The data shows that particles whose mobility diameter remains at 274 nm have an aerodynamic diameter of 1266 nm. In contrast, particles with electric-field-dependent mobility diameters have a d_{va} of 920 nm.

The set of measurements conducted on this mixture of hematite particles and presented in Figure 13 demonstrate that it is not only possible to distinguish symmetric particles from asymmetric ones, based on their behaviour in the DMA electric field, but that it is even possible to physically separate mixtures of particles according to their shapes.

3.6. *Particle morphology*

Above we have already described the application of a number of approaches to *simultaneously* measure and quantify several individual particles attributes. In this section we focus on the extension of these methods to characterise the morphological structure of individual particles, i.e. which substances are on the surface of the particle and whether they cover the surface partially or entirely.

Answering the question of which substance is on the surface is especially of interest for particles that contain organic substances. Recent field measurements have shown that organics comprise more than 50% of the aerosol mass in many regions around the world. The properties of particles that contain organics are subject to change during

heterogeneous reactions with the surrounding, oxidising atmosphere and the rates of these reactions strongly depend on whether the reacting substances are on the particle surface, or inside the particle, behind a protective shield. It is therefore important to determine not only what substances are present in the particles, but also which ones are on the particle surface.

The number of studies attempting to directly quantify particle morphology is very limited [25,47,109,110]. In all of these studies a laser(s) is used to 'drill' into the particles and characterise the morphological distribution of the particles' constituents based on the mass spectra obtained as a function of laser power. Unlike studies conducted by Carson *et al*. [109] and Woods *et al*. [110] that were carried out on supermicron particles with wide size distribution, we focused on much smaller particles with well defined core sizes and coating thicknesses.

In our first particle morphology study [47] we reported results from a mass spectroscopic study of 240 nm PSL spheres that were coated with $NaNO_3$, NaCl and sodium dodecyl sulphate (SDS) – all of which are sodium-containing substances. In these particle systems the known density of each component, together with the high resolution measurements of particle d_m and d_{va}, made it possible to calculate the thickness of the coating with 1 nm accuracy and investigate the dependence of the IPMS on the coating thickness. In this experiment the IPMS were generated with an excimer laser that was operated at two different fluences, 2.5 and 5 J/cm^2. These data showed that even for these small particles it is possible to use the dependence of the mass spectral intensity pattern on laser power to identify which of the substances are on the outside of the particle, and to simultaneously and quantitatively measure the particle composition, size, density and shape.

We demonstrated that the particle mass spectral signature depends not only on which substance is on the outside, but also on its morphological distribution on the spherical PSL bead. The data clearly showed that the PSL core of the particles that are homogeneously coated with $NaNO_3$ are more difficult to detect than when they are coated with NaCl or SDS that forms localised nodules on one side of the PSL particle. The morphology of NaCl-coated and SDS-coated PSL particles leaves a fraction of the PSL core exposed, making it easier to detect its ions. Note that in this study the coating layers were composed of Na-containing substances that have very high propensity to form positive ions.

Our second 'depth-profiling' study [25] was conducted on particles composed of a NaCl, inorganic core and coated with organic substances, which, most likely are better representatives of ambient atmospheric particles. The NaCl cores can, for example, be thought of as a surrogate for sea-salt particles. From a very different perspective, we note that the presence of a Na-containing core also provides an opportunity to investigate charge-transfer effects on mass spectra of internally mixed particles containing Na and semi-volatile organics. In this study liquid DOP and solid pyrene were used as the organic coatings. In Section 3.4 we already presented the study of the line shape of the vacuum aerodynamic size distributions of these particles and concluded that being liquid, DOP completely encapsulated the NaCl core to form spherical particles and that the solid pyrene condenses in localised nodules that together with the NaCl core form aspherical particles. We also used the mobility and aerodynamic diameter to calculate precisely particle sizes, DSF, densities and internal compositions. Here we focus on an investigation of the information content in the IPMS and their dependence on the laser power.

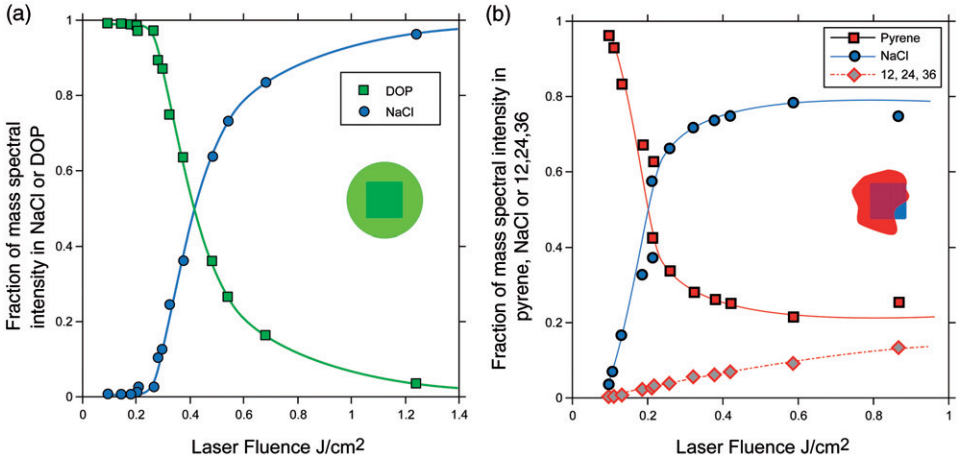

Figure 14. [Colour online] (a) A plot of the fraction of mass spectral peak intensity in the NaCl and DOP peaks as a function of laser fluence for NaCl particles with a 59 nm DOP coat; (b) A plot of the fraction of the mass spectral peak intensity in the NaCl, pyrene and carbon atoms (m/z=12, 24, 36) peaks as a function of laser fluence for the pyrene-coated NaCl seeds [25].

The goal is to show how observed changes mass spectral intensity patterns as a function of laser power can be used to unambiguously demonstrate that the organics are on the particle surface and probe if the coating covers the particle entirely or if it is localised in a small region, leaving some of the particles' NaCl cores exposed.

Figure 14(a) provides a graphic summary of changes in mass spectral intensities of the NaCl core and the DOP coating as a function of laser fluence for NaCl particles with a 59-nm-thick DOP coating. It shows that when the laser fluence is kept below 0.3 J/cm^2 the average mass spectra are dominated by DOP. Higher laser fluence yields deeper penetration through the DOP coating, as is evident by the increase in NaCl mass spectral intensity. At the very high laser fluence the DOP mass spectral peak intensities decrease, becoming barely detectable. This behaviour provides a clear illustration of the charge-transfer effects that impact IPMS generated by laser ablation. At higher laser powers when a larger fraction of the Na atoms are ablated from the particle core, they successfully compete for charges with the organic fragments, resulting in a drastic decrease in the mass spectral intensities of the organic fraction. This process of charge-transfer reactions is possible because it takes place under conditions of close physical proximity of all the particle constituents within the ablation plume.

Just a reminder, in Section 2 and Figure 4(b) we presented mass spectra of the very same particles, but generated in the IR/UV mode, where we showed that the IR/UV approach significantly diminishes matrix and charge-transfer effects and results in high quality mass spectra of the non-volatile NaCl core and the volatile DOP coating.

The changes in mass spectral intensity patterns, shown in Figure 14(a), are consistent with our previous conclusion regarding the morphology of these particles: at low laser fluence, the DOP coat shields the NaCl core from the laser, making it 'invisible', at higher laser fluence, the DOP coat is penetrated to reveal the NaCl core. When more Na is

evaporated it competes with the organic fragments for charges and the mass spectra become dominated by Na^+ ions.

Figure 14(b) shows an analysis of the behaviour of the average mass spectral intensities of pyrene-coated NaCl particles as a function of laser fluence, subdivided into three fractions: NaCl, pyrene and the highly fragmented fraction of pyrene peaks in the form of $m/z = 12$, 24 and 36. Similar to the DOP-coating case we find that at low laser fluence the average mass spectra are dominated by the coating substance, pyrene, and the core intensity is increasing with laser fluence. The most significant difference between the mass spectra of pyrene and the DOP-coated NaCl particles is that in the pyrene case the NaCl mass spectral peaks carry considerable intensity even at the very low laser fluences. Moreover, even at these low laser powers, a slight increase in laser power results in a relatively rapid increase in the NaCl peak intensities. At high laser fluence the NaCl intensity represents only 80% of the overall mass spectral intensity, with pyrene peaks still present in the mass spectra. These observations are consistent with the expected behaviour for a case in which the coating substance does not entirely cover the core surface.

This study shows that the SPLAT/DMA system makes it is possible to measure particle size, shape, density, quantitative composition and obtained rather detailed information on particle morphology.

3.7. *Single particle hygroscopicity*

The vast majority of atmospheric particles contain hygroscopic compounds, like inorganic salts and acids, and even many organics that also interact with the atmospheric water vapour. At low RH these particles are often dry and aspherical. At higher RH they absorb water and undergo phase transitions, or deliquescence, forming droplets that grow in size by absorbing more water in response to increases in RH, or decrease in size as the RH is reduced. If the RH decreases below the efflorescence point they transform into solid particles again. At RH slightly above 100% some of the particles get activated and form cloud droplets. Which particles get activated and under what conditions strongly depends on its size and hygroscopic properties, which in turn are directly related to the particles' compositions. Since most atmospheric particles are internally mixed, their hygroscopic properties depend not only on which of the hygroscopic substances they are composed of, but also on what else is in the same particle and how much of it is present.

Aerosol particles impact climate by scattering light and in their action as CNN. As we briefly described above, changes in RH result in changes in particle size, phase, optical properties, and even lung deposition efficiency, all of which directly impact their role in climate change or health effects. Thus, to accurately model particles climatic and health impacts requires proper representation of their properties as a function of the atmospheric RH.

The particles hygroscopicity is most commonly expressed in terms of their hygroscopic growth factor (GF), which is measured using a humidified tandem differential mobility analyser (HTDMA) [111,112]. In a typical HTDMA system the first DMA that is operated at low RH is used to select a narrow d_m distribution of particles dried prior to sampling. These particles are then transported to a conditioning chamber that is held at RH of 85% or higher, where particles absorb water, deliquesce and grow. The size distribution of the humidified particles is then measured by a second DMA that is operated at the same high

RH as the conditioning chamber. The differences between the mobility diameter of the dry particles and the mobility diameter measured at high RH by the second DMA reflect the changes in particles shapes and sizes as a function of RH. The GF is defined as the ratio of the particles' diameter measured at high RH to the diameter of the same particles classified with the first DMA, at near zero RH. In addition to a shift in mobility diameter, for ambient particles, there is typically also a change in the shape of the mobility size distribution. The breadth of the size distribution of the humidified aerosol reflects the fact that most ambient aerosol contains particles with a range of compositions and hence GFs. In the absence of any other measure of particle composition the measured GFs are sometimes even used to infer approximate particle compositions.

To develop unambiguous understanding of the relationship between particle compositions and their interaction with water vapour requires coupled simultaneous measurements of particle compositions and hygroscopicities. A number of laboratory HTDMA studies were conducted to quantify hygroscopic properties of laboratory-generated pure and internally mixed particles made of inorganic salts, organics, elemental carbon and mineral dust [113,114]. Several HTDMA studies of ambient aerosol particles that were carried in parallel with measurements of aerosol composition using impactor sampling [115] and the aerodyne aerosol mass spectrometer [116] observed some correlations between ambient particle hygroscopicity and average aerosol chemical composition. Since these measurements provided only average aerosol composition of assemblies of particles, they could not be used to distinguish between internally and externally mixed particles and could therefore not properly quantify the relationship between particle hygroscopicity and particle complex compositions.

In an attempt to address this deficiency, the HTDMA system was combined with electron microscopy [103]: In this system, the HTDMA was used to select particles of different sizes and hygroscopic GFs for analysis of individual particle shape and composition by electron microscopy. The authors reported that they observed differences in particle composition and shape that were systematically correlated with particle hygroscopicity. While such an off-line technique can in many cases provide critically needed information that connects individual particle composition and hygroscopicity, it is inherently slow and labour intensive and as a result, yields statistically limited data.

In this section we describe the application of an experimental set-up that consists of HTDMA system coupled with SPLAT to explore the relationship between individual particle compositions and their hygroscopicities. In this study we demonstrated, for the first time, the capability to measure simultaneously, and in real-time the size, composition, density and hygroscopicity of individual ambient particles [24]. Note that, because under most conditions the number concentration of ambient particles that make it through the HTDMA is very low, to carry out such a study requires a SPMS with extremely high sensitivity [24,117].

Figure 15 illustrates an example of the HTDMA measurements. The size distribution of dry (RH $< 1\%$) particles with mobility diameter of 200 nm is labelled and marked by red histogram-bars. These monodisperse particles selected by the first DMA were subsequently humidified to $85 \pm 2\%$ RH and the resulting d_m distribution, which is marked by the blue histogram-bars, was obtained by scanning the second DMA. As is clearly evident from this scan, virtually all particles absorb some water and as a result their mobility diameters increase. The d_m distribution of the humidified particles shows

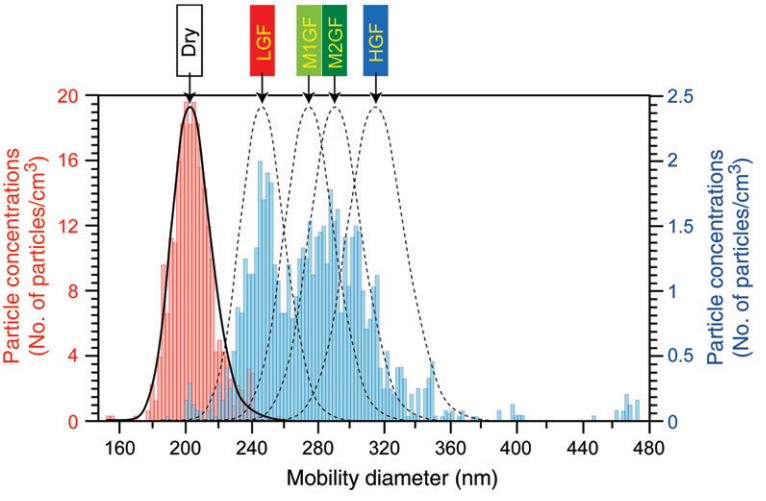

Figure 15. [Colour online] Measurements of particle hygroscopicity [24].

that the hygroscopic GFs of ambient particles range from ~1.2 to ~1.7. To measure the compositions and densities of particles with different GFs the second DMA was parked at each of the four positions that are labelled in Figure 15. The four GFs (low – LGF, two medium – M1GF and M2GF and high – HGF) were chosen in a way that assured that the entire size distribution was sampled by SPLAT as indicated by dashed lines representing the overlapping DMA distributions. Note the extremely low particle number concentrations indicated on the blue vertical scale on the right. These numbers represent the number concentrations of the particles that were selected by the second DMA and transmitted to SPLAT. During the ~5 h long experiment presented here we performed simultaneous measurements of individual particle GFs, compositions and densities for 3796 particles.

Figure 16 shows an example of mass spectra of four individual particles and lists their measured d_{va}, effective density and GF. In addition it displays the distribution of GFs of particles that belong to the same classes that each of these four particles was classified to. The first example is of a sea-salt particle in which sodium chloride was converted by atmospheric processing into sodium nitrate. It has an effective density of 1.73 g/cm^3 and a GF of 1.57. The measured GF and effective density of this particle are slightly lower than those expected for either pure NaCl or pure $NaNO_3$, which is consistent with the observation of mass spectral peaks that indicate the presence of some organics. The GF distribution bar graph shows that the majority of particles in this class exhibit medium and high GFs. The second particle is an example of biomass burning aerosol, with mass spectrum containing strong potassium peak and a wide range of organic components. It has-effective density of 1.4 g/cm^3 and an GF of 1.23. Potassium a containing particles, which are commonly found in the atmosphere, accounted for 20% of the particles with low GF in this study. The third particle containing vanadium and sodium is a processed sea-salt particle that absorbed vanadium, which is a by-product of oil combustion and was likely emitted by a ship. It has an effective density of 1.74 g/cm^3 and a GF of 1.57. The last

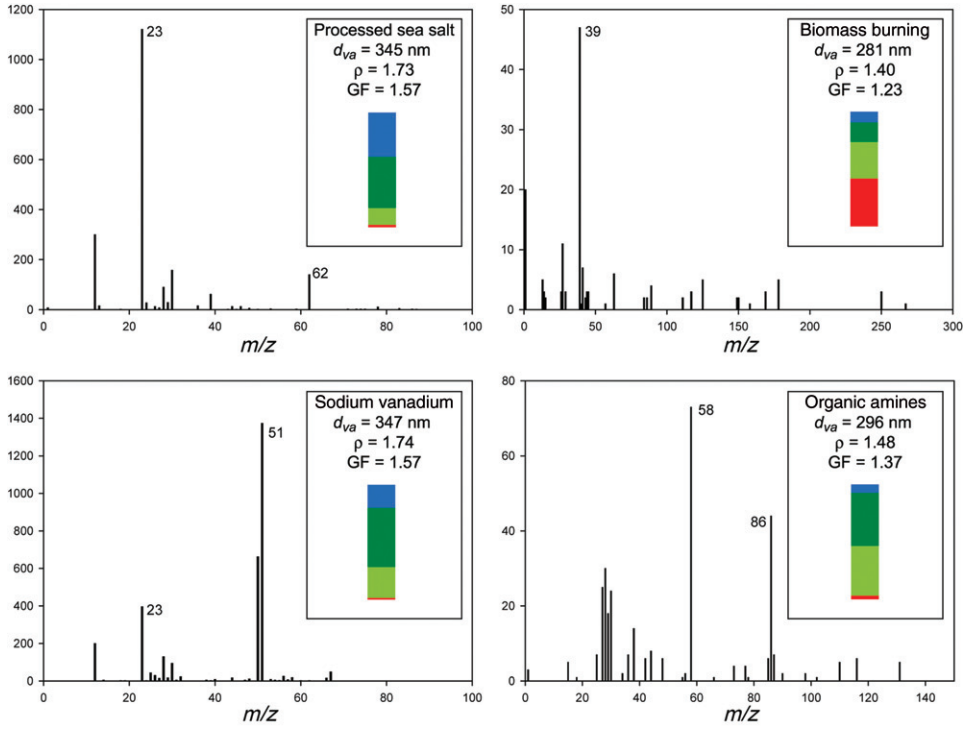

Figure 16. [Colour online] Mass spectra of four individual particles with dry d_m of 200 nm. Each frame also includes: a d_{va}, an effective density, and a GF. The bar graphs illustrate the GFs of other particles that belong to the same class as the displayed individual particle. Red, light green, dark green and blue indicate LGF, M1GF, M2GF and HGF, respectively, as marked in Figure 15 [24].

particle contains organic amines that are emitted by a wide range of anthropogenic and biogenic sources. It has an effective density of 1.48 g/cm^3 and a GF of 1.37. The GF distribution bar graph shows the GF of organic amines is ~1.4.

The majority (70%) of the particles characterised in this study were composed of sulphates that were internally mixed with organics (sulph/org). An examination of the measured properties of the sulph/org particles showed that their GFs and densities vary from particle to particle, reflecting differences in their internal compositions.

Figure 17 is a plot of the measured particle densities as a function of GFs for the internally mixed sulph/org particles showing that there is a tight correlation and simple relationship between the two. This trend is consistent with the observation that the mass spectra of particles of lower densities and GFs have more organics, since organics have lower densities and lower GFs compared to those of sulphate. The fact that the data show a relatively simple relationship between density and GF suggests that the types of organics that are mixed with sulphate do not change significantly from one particle class to the next, which was supported by the examination of IPMS.

The mass spectra of the sulph/org particles were classified into 11 classes, which have different average GFs and densities. As mentioned above, the average mass spectra of these 11 sulph/org classes revealed a simple trend: higher relative intensities of mass

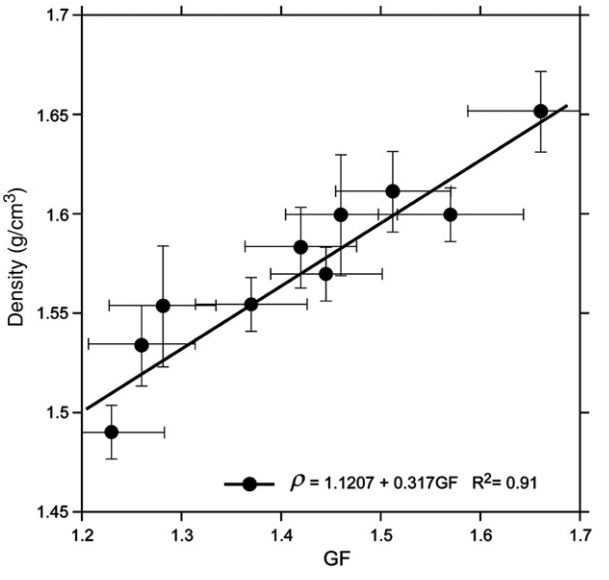

Figure 17. A plot of densities *vs* GFs observed for the particles that were classified into the 11 sulf/org classes [24].

spectral peaks that indicate the presence of organics are coupled to lower GF and density. An analysis of the mass spectral peaks indicated that oxygenated organics constitute the major fraction in each of these classes and that for the most part the differences between the classes are dominated by differences in the relative fraction of organics in these particles, although some variations in the compositions of the organic compounds between some of the classes were also present.

Finally, we use this comprehensive dataset of mass spectra, hygroscopicity and density of the particles belonging to the sulph/org class to illustrate that it also makes it possible to calculate the organic fraction in these particles. On the basis of the IPMS we determined that oxygenated organics constitute significant fraction of the particles' organic mass. The GFs of oxygenated organics can be estimated on the basis of the laboratory measured GFs for a number of organics that belong to this class and are commonly found in atmospheric particles [118]. The measured ambient particle GF can then be expressed using the commonly used Zdanovskii–Stokes–Robinson (ZSR) approximation, in which the organic and inorganic aerosol components are assumed to take up water independently [119]:

$$\mathrm{GF} = (\mathrm{VF}_{\mathrm{org}}\mathrm{GF}_{\mathrm{org}}^3 + (1 - \mathrm{VF}_{\mathrm{org}})\mathrm{GF}_{\mathrm{in}}^3)^{1/3}, \tag{6}$$

where $\mathrm{VF}_{\mathrm{org}}$ and $\mathrm{VF}_{\mathrm{in}}$ are the volume fractions of the organic and inorganic fractions in the dry particle, respectively, and $\mathrm{GF}_{\mathrm{org}}$ and $\mathrm{GF}_{\mathrm{in}}$ are the GFs of the organic and inorganic fractions, respectively [120,121].

Based on the GFs measurements of a number of oxygenated organics [118] we estimated $\mathrm{GF}_{\mathrm{org}}$ to be between 1.05 and 1.10, while the known GF of ammonium sulphate at 85% RH is 1.58 ± 0.04. As an illustrative example here we calculate the volume

fractions of the organics in the first ($GF_1 = 1.44$, $\rho_{eff1} = 1.58\,g/cm^3$) and ninth sulph/org ($GF_9 = 1.39$, $\rho_{eff9} = 1.53\,g/cm^3$) classes and find them to be $35\% \pm 2\%$ and $47\% \pm 2\%$, respectively. Based on the measured particle densities and the volume fractions, and assuming particle sphericity and volume additivity we calculate for the organic fractions densities of $1.22 \pm 0.03\,g/cm^3$ and $1.27 \pm 0.02\,g/cm^3$ for these two classes, respectively. These densities are consistent with known densities of laboratory generated SOAs [72,75,76,122] and estimated densities of ambient organics sampled at several locations [123]. Taken together, the calculated volume fractions and densities yield weight fractions of $27\% \pm 2\%$ and $38\% \pm 2\%$ for the organic in the first and ninth sulph/org classes, respectively.

4. Data analysis

The SMPS in general and SPLAT II, in particular, generate vast amounts of data, making data analysis a challenging task. What makes the analysis of IPMS particularly difficult is the fact that they are of high dimensionality.

SPLAT II can characterise hundreds of thousands of particles per day, generating vast amounts of rich and complex data that, as noted above, contain information on particle size, composition, density, hygroscopicity, shape, etc. In addition, these data often need to be analysed with respect to other observables, like time of day, altitude, wind speed, concentrations of gas phase pollutants, microphysical properties of clouds and many others. To make use of these vast and detailed data calls for dedicated software designed to transform the process of data mining of hundreds of gigabytes of data into a tractable task.

The first step in the analysis of SPMS data must clearly involve some kind of data organisation, where millions of IPMS are classified into different classes or clusters based on the similarity of their IPMS. Several data clustering approaches have been applied to the analysis of data produced by SPMSs [26–31,34,37,124,125]. These methods typically treat the IPMS as multidimensional vectors and calculate their proximity in N-D space using different distance metrics and clustering algorithms. At the conclusion of the classification process each class is represented by an average/representative mass spectrum. A common feature of most of these approaches is that once the data are organised and reduced into classes, there is no convenient path to a higher or lower level of details.

Moreover, a common assumption is that the SMPS data must be reduced to the point where the task of data comprehension becomes manageable. Hence, the data are typically classified into a small number of classes ($\sim$10), each represented by an average/representative spectrum, resulting in enormous loss of highly detailed and useful information.

Our goal was to develop methods that provide a flexible organisation of our datasets, containing millions of IPMS, in which no detail is lost and yet data mining remains tractable.

4.1. *SpectraMiner*

To this end we developed SpectraMiner, a data mining and visualisation software package that makes it possible to handle hundreds or thousands of clusters, limiting loss of

information and thus overcoming the boundaries set by traditional data cluster analysis approaches [31]. SpectraMiner presents the organised data in a circular interactive hierarchical tree, or dendogram, and provides the user with a visually driven, intuitive interface to easily access the data at all levels and, most importantly, to mine and visualise the data in real-time. The mass spectral data can be viewed on any level of detail, from the IPMS to the average mass spectrum of the entire dataset, and any intermediate point. SpectraMiner makes it possible to account for the complex internal mixtures of atmospheric aerosol particles without having to assign single particles to several classes, using partial membership, as it is done in a fuzzy classification algorithm. With SpectraMiner the user can easily find classes that contain very few particles of interest, create different dynamic views that illustrate the temporal evolution of the data, or the behaviour of the particle data as a function of any other variable of interest. SpectraMiner calculates and displays the correlations between different particle classes, which often indicate common sources. These are but a few examples of the numerous features of this software. Most importantly, they are all visually driven and are calculated and displayed in real-time.

Figure 18 shows one of SpectraMiner's annotated visual displays. The table in the top left corner offers the scientist the option to set the time period and particle size range of interest to be included in the display. The next table is used to specify the dendogram display parameters.

At the centre is the hierarchical tree – circular interactive dendogram, in which the classified and organised data are displayed. In the present case the dendogram includes 36,000 IPMS of 12 types of laboratory-generated particles. These particle types were chosen to represent some of the generic problems that are often encountered in laser ablation-based single particle mass spectroscopy of atmospheric particles. The points labelled clusters contain particles with similar IPMS. In this case the data were classified into the 62 numbered clusters that contain more than 20 particles. The dendogram radius is a true measure of IPMS similarity. Moving from the circumference, where the clusters are located, towards the centre amounts to reducing the similarity requirements for particles to be grouped together. As a result of the relaxed requirement for the IPMS similarity, similar clusters are merged together to form nodes, similar nodes merge together to form larger nodes, until eventually all IPMS in the dataset are merged together, forming the root node at the centre of the dendogram. Hence, clusters with similar particles merge rapidly and clusters containing very different particles do not merge until the centre of the circle, root node, is reached. The information on the particle content of any cluster or node becomes immediately available at the click of the mouse on a cluster or node of interest.

The 'tree branches' are coloured to indicate the number or percentage of particles they carry, using a rainbow colour map with a log(log(population)) colour scale. This scale makes it easy to instantly recognise clusters with many particles (red) or the presence of even sparsely populated clusters (blue).

The linear strip above the dendogram is the projection of clusters' populations. The small rectangles represent the population of the corresponding cluster at the circumference of the dendogram. The structure above the projection was added to illustrate which clusters are merged to form the main nodes that are alphabetically labelled in the dendogram in Figure 18. Like the dendogram, this view is interactively explorable.

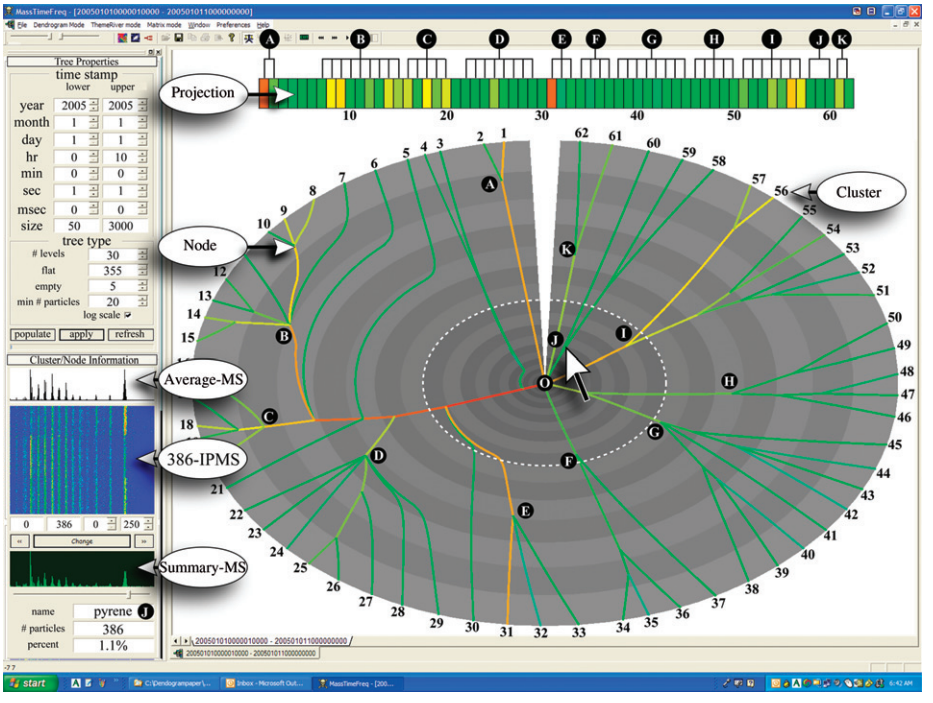

Figure 18. [Colour online] An annotated screen capture of a SpectraMiner visual display. At the centre is the dendogram and above it is a linear projection of clusters populations. On the top left is a table describing the dendogram input parameters and below is a graphic display of the mass spectral information of node J [31].

Here we chose 11 main nodes and alphabetically labelled them to define the important bifurcation points in each of the 11 branches. These 11 nodes were selected on the basis of a visual inspection of the entire classification tree. It is important to note that the key nodes are located on a wide range of radii, illustrating the fact that we have the option to explore the data with flexible similarity requirements.

Data mining begins by examining the content of the 11 key nodes shown in Figure 18. To explore the content of a cluster or node one simply clicks on the corresponding point on the dendogram and the program generates the graphic and tabular information shown in the lower left side of Figure 18 under the heading 'Cluster/Node Information'. Here we illustrate the outcome of clicking the mouse on the node labelled J. The program displays the average mass spectrum of all the particles in this node, which can easily be assigned to pyrene by making use of the interactive display readout of the mass spectral peak positions.

Below the average mass spectrum the program displays a scrollable pixel-map of all the 386 IPMS that populate this node. It is constructed from 386 horizontal lines, one for each of the IPMS, and the mass spectral peak intensities are indicated by colour, with red being high and blue being low. An overall view of the 'mosaic' in this panel reveals three distinct regions that correspond to three different fragmentation patterns of pyrene particles, one for each of the three clusters, 58, 59 and 60, that merge to form node J.

The table below the pixel-map summarises the information about the cluster/node being explored, the cluster/node name, the number of particles and their fraction.

A careful examination of the content of the 11 nodes clearly reveals that a number of them contain more than one particle type, and that a number of the nodes have particles of the same type. It is beyond this publication to provide a detailed description of the steps that need to be followed to improve on this preliminary result, but it is clear that significant improvements can be made simply by following the classification tree to the finer classification stages.

The measurements of the organic content of ambient particles represent a particularly challenging aspect of SPMS. In this model study we showed that for organic particles it was possible to significantly improve their identification by going to the cluster level.

Similar conclusions were reached for particles composed of sulphates internally mixed with organics that represent a very significant fraction of atmospheric aerosols. Here we generated and analysed the IPMS of the internally mixed ammonium sulphate and succinic acid particles and found the results of classification, at the major nodes level, to be rather poor, but achieved significant improvements at the cluster level.

Examination of the results for particles composed of NaCl and sodium nitrate revealed that the large Na^+ ion intensity makes separation between these two particle types by traditional, unsupervised statistical means almost impossible. However, we showed, in that study, that it is possible to overcome the limitation of statistics by introducing scientific 'expert' knowledge to guide the classification process, which brings us to the ClusterSculptor, our expert driven data classification software.

4.2. *ClusterSculptor*

The model study briefly presented in the previous section [31] demonstrated that data organisation that is exclusively driven by statistical metrics fails to properly separate particle types, and often spreads identical particles over a number of clusters, both of which hinder SMPS data analysis.

It is clear that the vast amount of expert knowledge, accumulated by scientist can and should be harnessed to help guide data classification, allowing the clustering process to take into account the peculiarities of the instruments used to acquire the data and the properties of the particles under study [27–29,31,124,126].

The most common way scientific expert knowledge is used to steer data classification is by manually combining clusters on the basis of their average mass spectra [27,126]. In some cases characteristic peaks are used to guide particle assignment to specific classes [31,124]. In a few cases data are modified prior to classification [27,29,31]. The efficacy of these approaches is difficult to estimate because they were mostly applied to ambient samples, of unknown compositions.

The results of the few studies that included classification of laboratory generated particles are briefly summarised here. Phares *et al.* [127] described the application of the ART-2a algorithm to data classification of seven laboratory generated particle types and concluded that many of them were poorly classified. Murphy *et al.* [27] conducted a study aimed at using particles of known compositions, to test their hierarchical clustering algorithm and to compare it with ART-2a algorithm [28,30]. In the Murphy *et al.* [27] study 'expert' knowledge was used to determine stopping conditions, choose data scaling,

and to 'manually' combine clusters. The final classification results revealed that expert input significantly improved data classification, but problems with ammonium sulphate, ammonium nitrate, organics and their mixtures still remained unsolved. Moffet and Prather [126] described results of using the ART-2a algorithm to classify two particle types – one composed of PSL and the other of dioctyl sebacate (DOS). IPMS of these particles were first classified using the ART-2a into 35 clusters, which were then hand sorted by placing all mass spectra with high intensity in the Na^+ in the DOS cluster and the rest into the PSL class. It is worth noting that of the two, only PSL particles are supposed to contain sodium. The authors justified this process by stating that, in their system, DOS particles contained sodium contaminations.

The very few cases where 'expert' input was used showed potential for improvements, despite being implemented in the absence of any intuitive tools that ease, guide, test and verify the data classification process. Our goal was to create a software package in which the scientist is placed at the centre of the classification process. To that end we have developed a software package we call ClusterSculptor [32,33] that is designed to provide the users with the tools to input their expert knowledge by sculpting the data in a manner that steers the clustering process. The software is interactive, intuitive and visually driven. The users can sculpt the data with a variety of tools, visually inspect the transformation using a number of data visualisation displays, modify the process and re-cluster the data, all of which are carried out with ease, and in real-time.

At present, data classification and exploration with SpectraMiner takes place in two steps. The classified data are first explored in SpectraMiner to identify cases that need to be improved by including expert knowledge in the clustering process. These data are exported to ClusterSculptor, reclassified and imported back to SpectraMiner for final analysis in the context of the entire dataset.

ClusterSculptor can also be used as a standalone real-time, expert driven, data classification program. It can directly classify datasets of as many as 30,000 IPMS. And, in cases where the datasets are larger, it first runs a simple statistical classification of the entire dataset to select a representative sample that contains 30,000 IPMS. The user then uses ClusterSculptor to expertly classify the selected 30,000 IPMS, at the end of which the entire dataset is organised into the user-created clusters. Below we provide a brief description of ClusterSculptor.

Figure 19 is a screen capture of ClusterSculptor displaying 7076 IPMS of particles containing ammonium sulphate and organics. At the centre, the program displays all of the 7076 IPMS in a colour map similar to the one used in SpectraMiner. Each horizontal line represents normalised IPMS, in which peak intensities are indicated by coloured pixels using the rainbow colour scheme, with red being high intensity and blue being low. Here we also use a log(log(peak intensity)) scale to enhance the presence of very low intensity peaks, making it easy to observe variations between IPMS. The IPMS in Figure 19 are grouped into several clusters that were created at one of the intermediate stages of the data classification. The mass spectra within each cluster are organised according to their distance to the centre of the cluster, but users can also sort the data by mass spectral intensity of any m/z value, by particle size or by acquisition time. The program allows the user to select the range of m/zs, particle sizes and time of acquisition to be displayed, providing an option to zoom into the data. In the lower panel, the program displays the unaltered average mass spectrum of the active cluster and at the top – the average sculpted

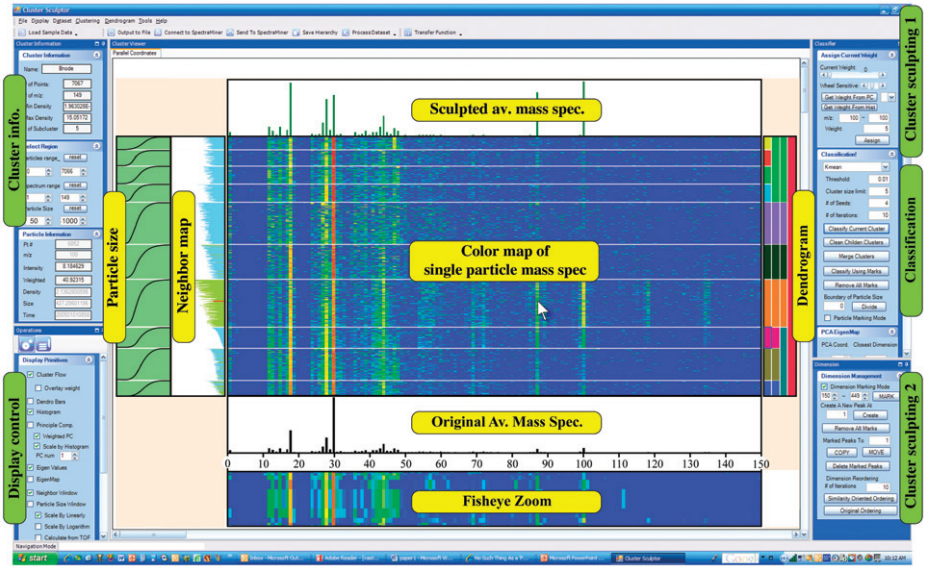

Figure 19. [Colour online] Screen capture of ClusterSculptor displaying 7,076 IPMS [33].

mass spectrum. The program provides the means to assign different 'weights' to the mass spectral peaks, which alter their intensities, and to create new peaks on the basis of existing ones. The most common use of the latter is the creation of a 'new' peak by first summing the intensities of a number of related peaks and then placing the value of the calculated sum at an m/z that typically has zero intensity. This option provides the means to minimise noise in the mass spectral relative peak intensities due to variations in fragmentation patterns.

Double clicking on any of the clusters makes it active, at which point all the displayed information in the cluster information window relates to this cluster. The dendogram, shown on the right, represents the cluster hierarchy. Based on visual examination the user can subdivide or merge any of the clusters on any level of the hierarchical tree until satisfactory results are achieved. In the lower window on the left, the program provides the users with various display options, like particle sizes, 3-D Eigen map of the IPMS, principal component window, etc.

On the right, the program displays the different sculpting control parameters. The bottom right window is used to sculpt the data by creating 'new' peaks on the basis of existing ones and the top right window is used to sculpt the data by assigning weights to selected peaks, thus changing their importance during data classification. The mass spectral peak intensities can be modified at any stage of the clustering process.

The classification control window is used to set the clustering criteria, such as distance metrics, minimum number of particles per cluster, minimum (threshold) distances, the number of clusters to be formed (for K-mean clustering) and number of iterations.

Successful application of ClusterSculptor to a number of particle types that are of interest to atmospheric science were presented in a previous publication describing a laboratory test case for SpectraMiner [31]. Below we present one illustrative example.

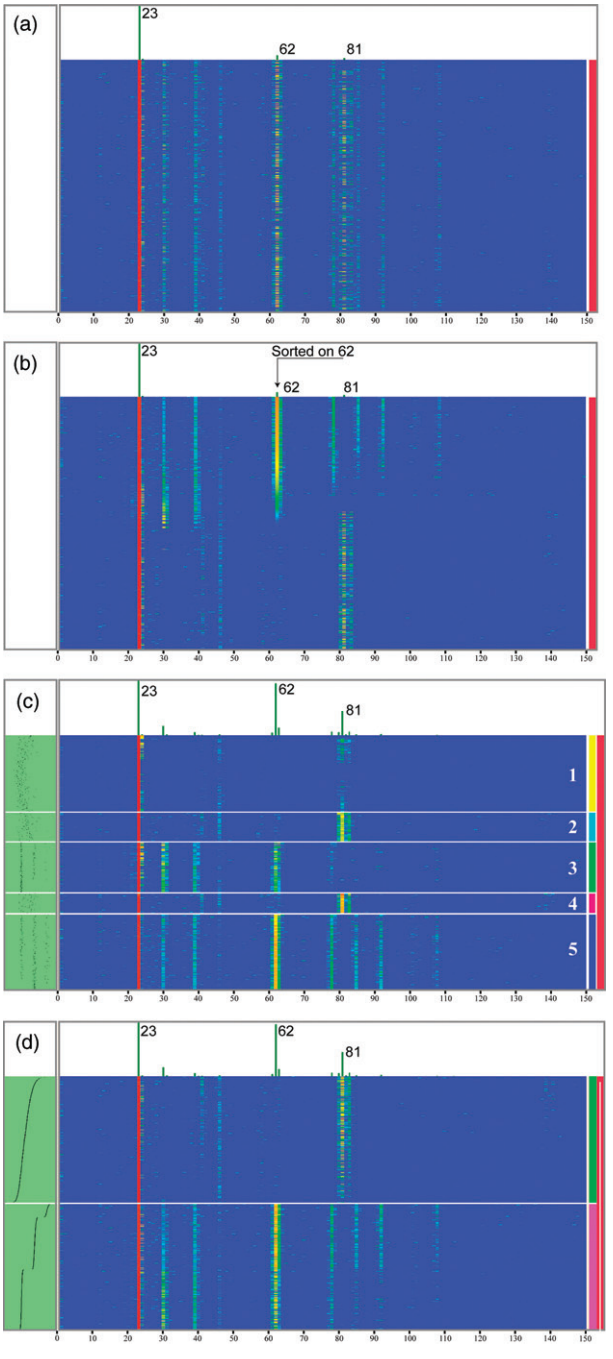

Figure 20. (a) A colour map of 3000 NaCl and 3000 $NaNO_3$ particles. (b) The same colour map but sorted according to the intensity of the peak at $m/z = 62$. (c) The average mass spectrum of the sculpted data (top). The colour map indicating the five clusters the data were classified into and the resulting dendrogram (right). The particle vacuum aerodynamic sizes (left green panel). (d) The final two clusters produced by recombining the five clusters in (c). Here the data are sorted by particle size [33].

In ablation-generated IPMS the presence of alkali metals results in mass spectra dominated by those ions [25,47–49]. Consequently, unsupervised data classification fails to separate different types of alkali metal-containing particles, like freshly emitted sea-salt particles composed of NaCl and processed sea-salt particles composed of $NaNO_3$. We noted above that the examination of the classification results in SpectraMiner revealed that in the absence of expert input NaCl and $NaNO_3$ were classified into the same clusters. Here we demonstrate the application of ClusterSculptor to the very same dataset.

The colour map of 3000 NaCl particles and 3000 $NaNO_3$ particles in Figure 20(a) shows that all the particles contain Na^+, but provides no clear indication that two distinct particle types are present. To explore the data content we reorder the data on the basis of the intensity at $m/z = 62$ and display the results in Figure 20(b), where the presence of two particle types is clearly revealed.

In order to improve the clustering process, we increase the weight of all mass spectral peaks with $m/z > 23$ from a default value of 1–10, i.e. increasing their intensity by a factor of 10. The resultant, sculpted data are classified into five clusters using K-mean clustering and presented in Figure 20(c).

A simple inspection of the IPMS in these five clusters indicates that the third (green) and fifth (blue) clusters contain $NaNO_3$ particles and that the other three are NaCl particles. To complete the data organisation, the clusters are combined accordingly to produce the two clusters shown in Figure 20(d), where the data are sorted by particle size. The classification process is complete and the two new clusters are ready to be exported back to SpectraMiner. It is important to note that the entire process of exporting the data from SpectraMiner, data visualisation, sculpting, clustering, merging and exporting the new clusters back to SpectraMiner is carried out in real-time and requires only a few minutes to complete.

We have carried out similar treatment on eight of the 12 particle types used in this study and demonstrated that ClusterSculptor greatly improves chemical speciation of single particles by introducing expert input into data classification process. The number of clusters representing the eight particle types was significantly reduced and most importantly, the new clusters are nearly pure.

5. Conclusions

Our goal was to develop new capabilities that will make it possible to characterise, in addition to individual particle size and composition, a wide range of particle properties. To this end we designed and constructed SPLAT II, a SPMS that offers advances over any other existing SPMS in a number of areas. SPLAT II has very high particle detection sensitivity, particularly to small particles, making it possible to characterise particles as small as 50 nm. It provides a very high sampling rate, and sizes particles with extremely high precision.

We showed that the high sizing resolution coupled with improved instrument sensitivity makes it possible to conduct experiments on DMA, TDMA and HTDMA classified particles. We illustrated that these types of measurements have the potential to provide direct information on particle size, density, effective density, DSF, asphericity, asymmetry, morphology, fractal dimension, hygroscopicity and quantitative compositions.

To take advantage of the large amounts of multidimensional data produced by SPLAT we developed novel approaches for data classification, visualisation and analysis. ClusterSculptor is a data classification program that offers a wide variety of intuitive, interactive, and visually driven tools that are combined with scientific expert knowledge to steer and refine the data classification process. SpectraMiner is a visually driven data mining program that makes it possible to explore datasets of millions of particles without loss of information and investigate relationships between different particle classes and between particles and any other data that were concurrently collected.

Acknowledgements

We thank all our co-authors and collaborators on the studies described in this review. This work was supported by the US Department of Energy Office of Basic Energy Sciences, Chemical Sciences Division, and Energy Efficiency and Renewable Energy. This research was in part performed in the Environmental Molecular Sciences Laboratory, a national scientific user facility sponsored by the Department of Energy's Office of Biological and Environmental Research at Pacific Northwest National Laboratory (PNNL). PNNL is operated by the US Department of Energy by Battelle Memorial Institute under contract No. DE-AC06-76RL0 1830.

References

[1] S. J. Ghan and S. E. Schwartz, Bull. Am. Meteorol. Soc. **88**, 1059 (2007).
[2] J. T. Houghton, Y. Ding, D. J. Griggs, M. Noguer, P. J. van der Linden, X. Dai, K. Maskell, and C. A. Johnson, IPCC Climate Change 2007, IPCC Fourth Assessment Report, 2007.
[3] A. N. Goldstein, C. M. Echer, and A. P. Alivisatos, Science **256**, 1425 (1992).
[4] L. Manna, D. J. Milliron, A. Meisel, E. C. Scher, and A. P. Alivisatos, Nat. Mater. **2**, 382 (2003).
[5] X. G. Peng, L. Manna, W. D. Yang, J. Wickham, E. Scher, A. Kadavanich, and A. P. Alivisatos, Nature. **404**, 59 (2000).
[6] P. H. McMurry, Atmospheric Environment. **34**, 1959 (2000).
[7] H. Coe and J. Allan, in *Analytical Techniques for Atmospheric Measurement*, edited by D. Heard (Blackwell Publishing, London, 2006).
[8] M. V. Johnston, J. Mass Spectrom. **35**, 585 (2000).
[9] D. M. Murphy, Mass Spectrom. Rev. **26**, 150 (2007).
[10] C. A. Noble and K. A. Prather, Mass Spectrom. Rev. **19**, 248 (2000).
[11] R. C. Sullivan and K. A. Prather, Anal. Chem. **77**, 3861 (2005).
[12] A. Zelenyuk and D. Imre, Aerosol Sci. Technol. **39**, 554 (2005).
[13] K. P. Hinz and B. Spengler, J. Mass Spectro. **42**, 843 (2007).
[14] D. G. Nash, T. Baer, and M. V. Johnston, International J. Mass Spectrom. **258**, 2 (2006).
[15] D. T. Suess and K. A. Prather, Chem. Rev. **99**, 3007 (1999).
[16] A. Zelenyuk, J. Yang, D. Imre, and E. Choi, Aerosol Sci. Technol. **43**, 411 (2009).
[17] A. Zelenyuk, Y. Cai, and D. Imre, Aerosol Sci. Tech. **40**, 197 (2006).
[18] A. Zelenyuk and D. Imre, Aerosol Sci. Technol. **41**, 112 (2007).
[19] A. Zelenyuk, Y. Cai, L. Chieffo, and D. Imre, Aerosol Sci. Tech. **39**, 972 (2005).
[20] A. Zelenyuk, J. Yang, C. Song, R. Zaveri, and D. Imre, Environ. Sci. Technol. **42**, 8033 (2008).
[21] A. Zelenyuk, L. A. Cuadra-Rodriguez, D. Imre, S. Shimpi, and A. Warey, in *Eos Trans. AGU*, Abstract A43A-0121, 2006.
[22] G. Buzorius, A. Zelenyuk, F. Brechtel, and D. Imre, Geophys. Res. Lett. **29**, 1974 (2002).
[23] A. Zelenyuk, D. Imre, L. A. Cuadra-Rodriguez, and B. Ellison, J. Aerosol Sci. **38**, 903 (2007).

[24] A. Zelenyuk, D. Imre, J. H. Han, and S. Oatis, Anal. Chem. **80**, 1401 (2008).
[25] A. Zelenyuk, J. Yang, C. Song, R. A. Zaveri, and D. Imre, J. Phys. Chem. A. **112**, 669 (2008).
[26] K. P. Hinz, M. Greweling, F. Drews, and B. Spengler, J. Am. Soc. Mass Spectrom. **10**, 648 (1999).
[27] D. M. Murphy, A. M. Middlebrook, and M. Warshawsky, Aerosol Sci. Technol. **37**, 382 (2003).
[28] D. J. Phares, K. P. Rhoads, A. S. Wexler, D. B. Kane, and M. V. Johnston, Anal. Chem. **73**, 2338 (2001).
[29] T. P. Rebotier and K. A. Prather, Anal. Chim. Acta. **585**, 38 (2007).
[30] X. H. Song, P. K. Hopke, D. P. Fergenson, and K. A. Prather, Anal. Chem. **71**, 860 (1999).
[31] A. Zelenyuk, D. Imre, Y. Cai, K. Mueller, Y. P. Han, and P. Imrich, Int. J. Mass Spectrom. **258**, 58 (2006).
[32] E. J. Nam, Y. Han, K. Mueller, A. Zelenyuk, and D. Imre, presented at the *IEEE Symposium on Visual Analytics Science and Technology*, Washington, DC, *VAST 2007*, 2007, p. 75.
[33] A. Zelenyuk, D. Imre, E. J. Nam, Y. Han, and K. Mueller, Int. J. Mass Spectrom. **275**, 1 (2008).
[34] A. Trimborn, K. P. Hinz, and B. Spengler, Aerosol Sci. Technol. **33**, 191 (2000).
[35] E. S. Cross, J. G. Slowik, P. Davidovits, J. D. Allan, D. R. Worsnop, J. T. Jayne, D. K. Lewis, M. Canagaratna, and T. B. Onasch, Aerosol Sci. Technol. **41**, 343 (2007).
[36] Y. X. Su, M. F. Sipin, H. Furutani, and K. A. Prather, Anal. Chem. **76**, 712 (2004).
[37] N. Erdmann, A. Dell'Acqua, P. Cavalli, C. Gruning, N. Omenetto, J. P. Putaud, F. Raes, and R. Van Dingenen, Aerosol Sci. Technol. **39**, 377 (2005).
[38] W. D. Reents, S. W. Downey, A. B. Emerson, A. M. Mujsce, A. J. Muller, D. J. Siconolfi, J. D. Sinclair, and A. G. Swanson, Aerosol Sci. Technol. **23**, 263 (1995).
[39] K. P. Rhoads, D. J. Phares, A. S. Wexler, and M. V. Johnston, J. Geophys. Res.-Atmos. **108**, 8418 (2003).
[40] P. Liu, P. J. Ziemann, D. B. Kittelson, and P. H. Mcmurry, Aerosol Sci. Technol. **22**, 293 (1995).
[41] P. Liu, P. J. Ziemann, D. B. Kittelson, and P. H. Mcmurry, Aerosol Sci. Technol. **22**, 314 (1995).
[42] J. T. Jayne, D. C. Leard, X. F. Zhang, P. Davidovits, K. A. Smith, C. E. Kolb, and D. R. Worsnop, Aerosol Sci. Technol. **33**, 49 (2000).
[43] A. Zelenyuk, D. Imre, and L. A. Cuadra-Rodriguez, Anal. Chem. **78**, 6942 (2006).
[44] J. A. Huffman, J. T. Jayne, F. Drewnick, A. C. Aiken, T. Onasch, D. R. Worsnop, and J. L. Jimenez, Aerosol Sci. Technol. **39**, 1143 (2005).
[45] E. Gard, J. E. Mayer, B. D. Morrical, T. Dienes, D. P. Fergenson, and K. A. Prather, Anal. Chem. **69**, 4083 (1997).
[46] D. S. Thomson, M. E. Schein, and D. M. Murphy, Aerosol Sci. Technol. **33**, 153 (2000).
[47] Y. Cai, A. Zelenyuk, and D. Imre, Aerosol Sci. Technol. **40**, 1111 (2006).
[48] P. T. A. Reilly, A. C. Lazar, R. A. Gieray, W. B. Whitten, and J. M. Ramsey, Aerosol Sci. Technol. **33**, 135 (2000).
[49] D. S. Gross, M. E. Galli, P. J. Silva, and K. A. Prather, Anal. Chem. **72**, 416 (2000).
[50] Z. Z. Ge, A. S. Wexler, and M. V. Johnston, Environ. Sci. Technol. **32**, 3218 (1998).
[51] T. Baer, J. Cabalo, A. Zelenyuk, and R. E. Miller, Abstr. Papers Am. Chem. Soc. **217**, U145 (1999).
[52] J. Cabalo, A. Zelenyuk, T. Baer, and R. E. Miller, Aerosol Sci. Technol. **33**, 3 (2000).
[53] B. D. Morrical, D. P. Fergenson, and K. A. Prather, J. Am. Soc. Mass Spectrom. **9**, 1068 (1998).
[54] A. Zelenyuk, J. Cabalo, T. Baer, and R. E. Miller, Anal. Chem. **71**, 1802 (1999).
[55] A. Zelenyuk, J. Yang, and D. Imre, Int. J. Mass Spectrom. **282**, 6 (2009).
[56] I. N. Tang and H. R. Munkelwitz, J. Geophys. Res.-Atmos. **99**, 18801 (1994).
[57] Y. Katrib, S. T. Martin, Y. Rudich, P. Davidovits, J. T. Jayne, and D. R. Worsnop, Atmos. Chem. Phys. **5**, 275 (2005).

[58] S. V. Hering and M. R. Stolzenburg, Aerosol Sci. Technol. **23**, 155 (1995).
[59] P. H. McMurry, X. Wang, K. Park, and K. Ehara, Aerosol Sci. Technol. **36**, 227 (2002).
[60] H. Hasan and T. G. Dzubay, Atmos. Environ. **17**, 1573 (1983).
[61] M. Kalberer, J. Yu, D. R. Cocker, R. C. Flagan, and J. H. Seinfeld, Environ. Sci. Technol. **34**, 4894 (2000).
[62] G. Hanel and J. Thudium, Pure and Appl. Geophys. **115**, 799 (1977).
[63] L. Morawska, G. Johnson, Z. D. Ristovski, and V. Agranovski, Atmos. Environ. **33**, 1983 (1999).
[64] M. Pitz, J. Cyrys, E. Karg, A. Wiedensohler, H. E. Wichmann, and J. Heinrich, Environ. Sci. Technol. **37**, 4336 (2003).
[65] D. M. Murphy, D. J. Cziczo, P. K. Hudson, M. E. Schein, and D. S. Thomson, J. Aerosol Sci. **35**, 135 (2004).
[66] W. P. Kelly and P. H. Mcmurry, Aerosol Sci. Technol. **17**, 199 (1992).
[67] S. W. Stein, B. J. Turpin, X. P. Cai, C. P. F. Huang, and P. H. Mcmurry, Atmos. Environ. **28**, 1739 (1994).
[68] B. Schleicher, S. Kunzel, and H. Burtscher, J. Appl. Phys. **78**, 4416 (1995).
[69] A. Virtanen, J. Ristimaki, and J. Keskinen, Aerosol Sci. Technol. **38**, 437 (2004).
[70] J. L. Hand and S. M. Kreidenweis, Aerosol Sci. and Technol. **36**, 1012 (2002).
[71] P. F. DeCarlo, J. G. Slowik, D. R. Worsnop, P. Davidovits, and J. L. Jimenez, Aerosol Sci. Technol. **38**, 1185 (2004).
[72] R. Bahreini, M. D. Keywood, N. L. Ng, V. Varutbangkul, S. Gao, R. C. Flagan, J. H. Seinfeld, D. R. Worsnop, and J. L. Jimenez, Environ. Sci. Technol. **39**, 5674 (2005).
[73] M. T. Spencer, L. G. Shields, and K. A. Prather, Environ. Sci. Technol. **41**, 1303 (2007).
[74] M. R. Alfarra, D. Paulsen, M. Gysel, A. A. Garforth, J. Dommen, A. S. H. Prevot, D. R. Worsnop, U. Baltensperger, and H. Coe, Atmos. Chem. Phys. **6**, 5279 (2006).
[75] A. Zelenyuk, J. Yang, C. Song, R. A. Zaveri, and D. Imre, Environ. Sci. Technol. **42**, 8033 (2008).
[76] C. Song, R. A. Zaveri, M. L. Alexander, J. A. Thornton, S. Madronich, J. V. Ortega, A. Zelenyuk, X.-Y. Yu, A. Laskin, and D. A. Maughan, Geophys. Res. Lett. **34**, L20803 (2007).
[77] Y. Yu, M. J. Ezell, A. Zelenyuk, D. Imre, L. Alexander, J. Ortega, B. D'Anna, C. W. Harmon, S. N. Johnson, and B. J. Finlayson-Pitts, Atmos. Environ. **42**, 5044 (2008).
[78] D. J. Cziczo, J. B. Nowak, J. H. Hu, and J. P. D. Abbatt, J. Geophys. Res.-Atmos. **102**, 18843 (1997).
[79] J. M. Lightstone, T. B. Onasch, D. Imre, and S. Oatis, J. Phys. Chem. A. **104**, 9337 (2000).
[80] D. J. Cziczo and J. P. D. Abbatt, J. Phys. Chem. A. **104**, 2038 (2000).
[81] P. G. Dougle, J. P. Veefkind, and H. M. Ten Brink, J. Aerosol Sci. **29**, 375 (1998).
[82] I. N. Tang, in *Generation of Aerosols and Facilities for Exposure Experiments*, edited by K. Willeke (Ann Arbor Science Publishers Inc., Ann Arbor, MI, 1980), p. 153.
[83] C. B. Richardson and R. L. Hightower, Atmos. Environ. **21**, 971 (1987).
[84] I. N. Tang, J. Geophys. Res.-Atmos. **102**, 1883 (1997).
[85] R. C. Hoffman, A. Laskin, and B. J. Finlayson-Pitts, J. Aerosol Sci. **35**, 869 (2004).
[86] D. K. Song, I. W. Lenggoro, Y. Hayashi, M. Okuyama, and S. S. Kim, Langmuir. **21**, 10375 (2005).
[87] W. C. Hinds, *Aerosol Technology: Properties, Behavior, and Measurement of Airborne Particles* (Wiley-Interscience, New York, NY, 1999).
[88] P. A. Baron and K. Willeke, *Aerosol Measurement. Principles, Techniques, and Applications* (John Wiley and Sons Ltd, New York, NY, 2001), p. 1.
[89] X. F. Zhang, K. A. Smith, D. R. Worsnop, J. Jimenez, J. T. Jayne, and C. E. Kolb, Aerosol Sci. Technol. **36**, 617 (2002).

[90] Y. S. Cheng, M. D. Allen, D. P. Gallegos, H.-C. Yeh, and K. Peterson, Aerosol Sci. Technol. **8**, 199 (1988).
[91] Y. Kousaka, Y. Endo, H. Ichitsubo, and M. Alonso, Aerosol Sci. Technol. **24**, 36 (1996).
[92] Y. S. Cheng, M. D. Allen, D. P. Gallegos, H. C. Yeh, and K. Peterson, Aerosol Sci. Technol. **8**, 199 (1988).
[93] G. Scheuch and J. Heyder, J. Aerosol Sci. **17**, 432 (1986).
[94] M. D. Allen and O. G. Raabe, J. Aerosol Sci. **16**, 57 (1985).
[95] H. C. Hansson and M. S. Ahlberg, J. Aerosol Sci. **16**, 69 (1985).
[96] H. Horvath, Staub Reinhalt. Luft. **34**, 197 (1974).
[97] H. Horvath, J. Aerosol Sci. **10**, 309 (1979).
[98] B. Dahneke, Aerosol Sci. Technol. **1**, 179 (1982).
[99] P. Chan and B. Dahneke, J. Appl. Phys. **52**, 3106 (1981).
[100] W. D. Dick, P. J. Ziemann, P. F. Huang, and P. H. McMurry, Meas. Sci. Technol. **9**, 183 (1998).
[101] R. J. Perry, A. J. Hunt, and D. R. Huffman, Appl. Opt. **17**, 2700 (1978).
[102] L. Kramer, U. Poschl, and R. Niessner, J. Aerosol Sci. **31**, 673 (2000).
[103] P. H. McMurry, M. Litchy, P. F. Huang, X. P. Cai, B. J. Turpin, W. D. Dick, and A. Hanson, Atmos. Environ. **30**, 101 (1996).
[104] K. Park, F. Cao, D. B. Kittelson, and P. H. McMurry, Environ. Sci. Technol. **37**, 577 (2003).
[105] J. G. Slowik, K. Stainken, P. Davidovits, L. R. Williams, J. T. Jayne, C. E. Kolb, D. R. Worsnop, Y. Rudich, P. F. DeCarlo, and J. L. Jimenez, Aerosol Sci. Technol. **38**, 1206 (2004).
[106] J. A. Nelson, R. J. Crookes, and S. Simons, J. Phys. D-Appl. Phys. **23**, 465 (1990).
[107] D. Salcedo, T. B. Onasch, M. R. Canagaratna, K. Dzepina, J. A. Huffman, J. T. Jayne, D. R. Worsnop, C. E. Kolb, S. Weimer, F. Drewnick, J. D. Allan, A. E. Delia, and J. L. Jimenez, Atmos. Chem. Phys. **7**, 549 (2007).
[108] J. Schreiner, U. Schild, C. Voigt, and K. Mauersberger, Aerosol Sci. Technol. **31**, 373 (1999).
[109] P. G. Carson, M. V. Johnston, and A. S. Wexler, Aerosol Sci. Technol. **26**, 291 (1997).
[110] E. Woods, G. D. Smith, R. E. Miller, and T. Baer, Anal. Chem. **74**, 1642 (2002).
[111] B. Y. H. Liu, D. Y. H. Pui, K. T. Whitby, D. B. Kittelson, Y. Kousaka, and R. L. Mckenzie, Atmos. Environ. **12**, 99 (1978).
[112] D. J. Rader and P. H. Mcmurry, J. Aerosol Sci. **17**, 771 (1986).
[113] M. N. Chan and C. K. Chan, Atmos. Chem. Phys. **5**, 2703 (2005).
[114] A. Vlasenko, S. Sjogren, E. Weingartner, H. W. Gaggeler, and M. Ammann, Aerosol Sci. Technol. **39**, 452 (2005).
[115] M. L. Pitchford and P. H. Mcmurry, Atmos. Environ. **28**, 827 (1994).
[116] M. Gysel, J. Crosier, D. O. Topping, J. D. Whitehead, K. N. Bower, M. J. Cubison, P. I. Williams, M. J. Flynn, G. B. McFiggans, and H. Coe, Atmos. Chem. Phys. Discuss. **6**, 12503 (2006).
[117] G. Buzorius, A. Zelenyuk, F. Brechtel, and D. Imre, Geophys. Res. Lett. **29** (20), Art. No. 1974 (2002).
[118] V. Varutbangkul, F. J. Brechtel, R. Bahreini, N. L. Ng, M. D. Keywood, J. H. Kroll, R. C. Flagan, J. H. Seinfeld, A. Lee, and A. H. Goldstein, Atmos. Chem. Phys. **6**, 2367 (2006).
[119] J. H. Seinfeld and S. N. Pandis, *Atmospheric Chemistry and Physics: From Air Pollution to Climate Change* (Wiley, New York, NY, 1998), p. 1326.
[120] C. N. Cruz and S. N. Pandis, Environ. Sci. Technol. **34**, 4313 (2000).
[121] A. J. Prenni, P. J. De Mott, and S. M. Kreidenweis, Atmos. Environ. **37**, 4243 (2003).
[122] Y. Yu, M. Ezell, A. Zelenyuk, D. Imre, L. Alexander, J. Ortega, B. D'Anna, C. W. Harmon, S. N. Johnson, and B. J. Finlayson-Pitts, Atmos. Environ. **42**, 5044 (2008).

[123] B. J. Turpin and H. J. Lim, Aerosol Sci. Technol. **35**, 602 (2001).
[124] P. V. Tan, O. Malpica, G. J. Evans, S. Owega, and M. S. Fila, J. Am. Soc. Mass Spectrom. **13**, 826 (2002).
[125] K. P. Hinz, R. Kaufmann, and B. Spengler, Aerosol Sci. Technol. **24**, 233 (1996).
[126] R. C. Moffet and K. A. Prather, Anal. Chem. **77**, 6535 (2005).
[127] D. J. Phares, K. P. Rhoads, M. V. Johnston, and A. S. Wexler, J. Geophys. Res.-Atmos. **108**, 8420 (2003).